THE STRUCTURE OF MAGNETOHYDRODYNAMIC TURBULENCE

APPROVED BY
DISSERTATION COMMITTEE:

Supervisor: ______________________________

Supervisor: ______________________________

____

____

____

THE STRUCTURE OF MAGNETOHYDRODYNAMIC TURBULENCE

by

JUNGYEON CHO, B.S., M.S.

DISSERTATION

Presented to the Faculty of the Graduate School of

The University of Texas at Austin

in Partial Fulfillment

of the Requirements

for the Degree of

Doctor of Philosophy

THE UNIVERSITY OF TEXAS AT AUSTIN

May 2000

To my family

Acknowledgements

I want to express my special thanks to my advisor, Ethan Tecumseh Vishniac, for his great advice and help. I also want to thank John Scalo, Craig Wheeler, Matt Choptuik, and Fausto Cattaneo. I also thank all faculty members and staffs in the Astronomy Department of the University of Texas. I am also indebted by many people in Johns Hopkins University for helping me to work with Ethan Vishniac. Finally I thank my family.

THE STRUCTURE OF MAGNETOHYDRODYNAMIC TURBULENCE

Publication No. ______________

Jungyeon Cho, Ph.D.
The University of Texas at Austin, 2000

Supervisors: Ethan Tecumseh Vishniac
John M. Scalo

Magnetized astrophysical plasmas often exhibit turbulent motions. Such plasmas frequently can be described by magnetohydrodynamics (MHD). I have studied the structure of MHD turbulence numerically. I have performed direct 3-dimensional numerical simulations for MHD turbulence in a periodic box of size 2π threaded by uniform external magnetic fields. I have considered two extreme limits - strong external magnetic field limits and weak/zero external field limits. In the strong external field limits, I have analyzed the structure of eddies as a function of scale. The results are consistent with the scaling law proposed by Goldreich and Sridhar: smaller eddies are more elongated than larger ones. In the weak/zero external field limits, I have studied the structure and generation of magnetic fields. I have found that the magnetic fields are amplified through field line stretching at a rate proportional to the difference between the velocity and the magnetic field strength times a constant.

Equipartition between the kinetic and magnetic energy densities occurs at a scale somewhat smaller than the kinetic energy peak. Above the equipartition scale the velocity structure is, as expected, nearly isotropic. The magnetic field structure at these scales is uncertain, but the field correlation function is very weak. At the equipartition scale the magnetic fields show only a moderate degree of anisotropy, so that the typical radius of curvature of field lines is comparable to the typical perpendicular scale for field reversal. In other words, there are few field reversals within eddies at the equipartition scale, and no fine-grained series of reversals at smaller scales. At scales below the equipartition scale, both velocity and magnetic structures are anisotropic; the eddies are stretched along the local magnetic field lines.

Table of Contents

List of Tables

List of Figures

Chapter 1

Introduction

Since astrophysical fluids exhibit turbulent motions and magnetic fields are undoubtedly found in such fluids, magnetohydrodynamic (MHD) turbulence is an important field of study in astronomy. In most astrophysical plasmas, the magnetic Reynolds number easily exceeds 10^{10}. In such a system, the usual expectation is that magnetic field is frozen into the fluid. The velocity field advects and stretches magnetic field lines and magnetic field exerts pressure and tension forces on velocity fields. Therefore, in general, MHD turbulence is different from pure hydrodynamic turbulence.

In pure incompressible hydrodynamic turbulence, there exists a well-known empirical theory: Kolmogorov theory. Fully developed turbulence shows eddies of various sizes interacting each other. In Kolmogorov theory, kinetic energy contained in large scale eddies cascades down to small scale eddies within one eddy turnover time. Therefore, the rate of energy cascade at scale l is proportional to the kinetic energy (V_l^2) divided by eddy turnover time (l/V_l), where V_l is the r.m.s. velocity of eddies of size $\sim l$. In the inertial range this cascade rate should be scale-independent, which yields $V_l^3 \propto l$. From this and the relation $V_l \propto \sqrt{kE(k)}$, one can obtain the well-known Kolmogorov spectrum: $E(k) \propto k^{-5/3}$. Here, $E(k)$ is the one-dimensional energy spectrum. Kolmogorov theory agrees well with both experimental and numerical data at least as a first approximation. Although MHD turbulence has been studied for many decades, there is no well-agreed-upon theory. This is partly because laboratory measurements of MHD turbulence are relatively hard and rare. Therefore, numerical studies are highly desirable in MHD turbulence.

In this work, we study MHD turbulence through direct numerical simulations. We consider MHD turbulence in a periodic box of size 2π threaded by a uniform external magnetic field. We consider 2 extreme cases: strong external field cases and weak/zero external field cases. The presence of the external magnetic field breaks isotropy of the system and causes anisotropic structure. The anisotropic structure will depends on the strength of the external field.

When the external field is very strong, anisotropy will appear at the largest energy containing eddy scale (i.e. the scale where the turbulence is driven). This anisotropy results from the resonant conditions for 3-wave interactions or 4-wave interactions when 3-wave interactions are null (see §3.1). Several theories exist about anisotropy in this regime. Most of the theories predict a scale-dependent anisotropy: anisotropy is more pronounced at smaller scales. However, their detailed predictions are different from each other. In Chapter 3, we briefly review and numerically test such theories. The results are consistent with the scaling law $\tilde{k}_{\parallel} \sim \tilde{k}_{\perp}^{2/3}$ proposed by Goldreich and Sridhar (1995, 1997). Here, $\tilde{k}_{\parallel}$ and $\tilde{k}_{\perp}$ are proportional to the inverse of major and minor axis of eddies, respectively. Although its structure in Fourier space is completely different from that of pure hydrodynamic turbulence due to anisotropy, Goldreich and Sridhar's model predicts a Kolmogorov-like one-dimensional energy spectrum: $E(k) \propto k^{-5/3}$.

Numerical studies have already addressed this scale-dependent anisotropy (Shebalin et al. 1983; Oughton et al. 1994; Ghosh and Goldstein 1997; Matthaeus et al. 1998). However, all these works rely on indirect methods (see §3.1). We also note that none of the previous papers quantitatively compared their results with particular theories of anisotropy. On the other hand, there is some important observational evidence concerning the nature of MHD turbulence. Unfortunately it is all in the very low density regime, where the fluid approximation is suspect. However, there are in situ measurements of the solar wind which support a Kolmogorov-like power distribution on smaller scales and similar results (although less certain) for the ISM. Solar wind observations, which are well within the strongly magnetized regime, show an energy spectrum $E(k) \sim k^{-1.70}$ (Leamon et al. 1998). Observations of the density irregularities in the interstellar medium shows the existence of a Kolmogorov-like power-law spectrum (see, for example, Armstrong et al. 1995) This is an important piece of evidence in favor of Goldreich and Sridhar's model.

On the other hand, when the external magnetic field is weak/zero, we may expect isotropy at the largest energy containing scale. Anisotropy will emerge at some scales smaller than the largest energy containing scale. In Chapter 4, we test this idea and determine the scale below which turbulence becomes anisotropic. We also give empirical relations regarding the generation of magnetic fields in this regime.

Although this work concentrates on basic physical processes without direct reference to astrophysical objects, it will provide useful insights in constructing astrophysical models, e.g. mean-field dynamo theories.

The organization of this dissertation is as follows. In Chapter 2, we describe the numerical methods. In Chapter 3, we study anisotropy of MHD turbulence in the strong external magnetic field limit. In Chapter 4, we study the structure and generation of MHD turbulence in the weak/zero external field limit. In Chapter 5, we give summary and future study plan.

Chapter 2

Numerical Methods and Tests of the Code

We used a pseudo-spectral code to solve the MHD equations in a periodic box of size 2π:

$$\frac{\partial \mathbf{V}}{\partial t} = (\nabla \times \mathbf{V}) \times \mathbf{V} - (\nabla \times \mathbf{B}) \times \mathbf{B} + \nu \nabla^2 \mathbf{V} + \mathbf{f} + \nabla P', \tag{2.1}$$

$$\frac{\partial \mathbf{B}}{\partial t} = \mathbf{B} \cdot \nabla \mathbf{V} - \mathbf{V} \cdot \nabla \mathbf{B} + \eta \nabla^2 \mathbf{B}, \tag{2.2}$$

$$\nabla \cdot \mathbf{V} = \nabla \cdot \mathbf{B} = 0, \tag{2.3}$$

where $\mathbf{f}$ is a random forcing term with unit correlation time, $P' \equiv P + \mathbf{V} \cdot \mathbf{V}/2$, $\mathbf{V}$ is the velocity, and $\mathbf{B}$ is magnetic field divided by $(4\pi\rho)^{1/2}$. Thus the field $\mathbf{B}$ is, in fact, the Alfvénic velocity. The Alfvén velocity of the background field, B_0, is set to order unity in Chapter 3 and $10^{-3.5}$ or 0 in Chapter 4. Through out this work, we consider only cases where viscosity is equal to magnetic diffusivity:

$$\nu = \eta. \tag{2.4}$$

In the pseudo-spectral approach, the actual calculations are performed in wavevector space. The nonlinear terms are evaluated in real space using Fourier transformed variables and their derivatives and then transformed back into their

Fourier components. The forcing term consists of 21 Fourier components with $2 \leq k \leq \sqrt{12}$. The peak of energy injection is at $k \approx 2.5 (\equiv k_L)$. We adjusted the amplitudes of the forcing components so that $V \approx 1$. We use exactly same forcing terms for all simulations. Therefore, the external magnetic fields are comparable to the rms velocity ($B_0 \sim V$) in Chapter 3 and very weak ($B_0 \ll V$) in Chapter 4. Each forcing component consists of two parts: a linearly polarized component and a small circularly polarized component with a preferred helicity. The latter was introduced to provide non-zero helicity injection to the turbulence. The resulting fluid helicity is $0.3 \sim 0.4$ for all runs. However, our results are insensitive to the value of helicity, possibly because the box size is only slightly bigger than the energy injection scale. We use an appropriate projection operator to calculate the $\nabla P'$ term in Fourier space and also to enforce the divergence-free condition ($\nabla \cdot \mathbf{V} = \nabla \cdot \mathbf{B} = 0$). We use up to 256^3 collocation points. We use the integration factor technique for kinetic and magnetic dissipation terms and the leap-frog method for the nonlinear terms. At $t = 0$, the magnetic field is uniform and the velocity is spread between $2 \leq k \leq 4$ in wavevector space. We give the parameters for each run in Table 3.1 and Table 4.1.

Either physical viscosity (and diffusivity) or hyperviscosity (and hyperdiffusivity) is used in the dissipation terms (see Table 3.1 and 4.1). The power of hyperviscosity is set to 8, such that the dissipation term in the above equation is replaced with

$$-\nu_8 (\nabla^2)^8 \mathbf{V}, \tag{2.5}$$

where ν_8 is determined from the condition $\nu_h (N/2)^{2h} \Delta t \approx 0.5$ (see Borue and Orszag 1995,1996). Here Δt is the time step and N is the number of grids in each direction. The same expression is used for the magnetic dissipation term.

When $\mathbf{f} = \nu = \eta = 0$, that is, without forcing or dissipation, the total energy drops by 0.87 percent after 13 time units, apparently due to truncation errors. In the dissipative case the injection and dissipation of energy are well balanced after the magnetic energy reaches the stationary state:

$$< \epsilon > = < D_K > + < D_M >, \tag{2.6}$$

where ϵ is the energy injection rate and D_K and D_M are the kinetic and the magnetic energy dissipation rates respectively. The angle bracket stands for an appropriate space-time average, which is taken after the magnetic energy reaches the stationary state.

Before we describe the third test, we define several transfer functions. Imagine velocity components in a thin (i.e., thickness=1) spherical shell of radius k in Fourier space. The work done to the velocity components by magnetic fields can be written as follows:

$$-\sum_{k \le |\mathbf{p}| < k+1} \hat{\mathbf{V}}(\mathbf{p})^* \cdot [(\nabla \times \widehat{\mathbf{B}}) \times \mathbf{B}](\mathbf{p}), \tag{2.7}$$

where *hatted* variables are Fourier space variables and '*' denotes a complex conjugate. This relation is derived from the second term in right-hand side of equation (2.1). This quantity is the *negative* of the energy transferred to the magnetic fields from the velocity components per unit time:

$$T_{b|v_k}(k) = + \sum_{k \le |\mathbf{p}| < k+1} \hat{\mathbf{V}}(\mathbf{p})^* \cdot [(\nabla \times \widehat{\mathbf{B}}) \times \mathbf{B}](\mathbf{p}).. \tag{2.8}$$

Note that the subscripts of $T_{X|Y}$ read '*to X from Y*.' Similarly, from the first term in the right-hand side of equation (2.1), we obtain $T_{v|v_k}(k)$:

$$T_{v|v_k}(k) = - \sum_{k \le |\mathbf{p}| < k+1} \hat{\mathbf{V}}(\mathbf{p})^* \cdot [(\nabla \times \widehat{\mathbf{V}}) \times \mathbf{V}](\mathbf{p}). \tag{2.9}$$

Now, consider the magnetic components in the same shell. From the first term in the right-hand side of equation (2.2), we obtain the energy transferred to the velocity fields from the magnetic components per unit time:

$$T_{v|b_k}(k) = - \sum_{k \le |\mathbf{p}| < k+1} \hat{\mathbf{B}}(\mathbf{p})^* \cdot [\mathbf{B} \widehat{\cdot \nabla} \mathbf{V}](\mathbf{p}). \tag{2.10}$$

the work done to the magnetic components by velocity fields: Again, this quantity is the *negative* of the work done to the magnetic components by velocity fields per unit time.

In the third test, we checked the energy budget of the magnetic fields. The *net* energy transferred to magnetic fields from velocity fields can be calculated from either $T_{b|v_k}(k)$ or $T_{v|b_k}(k)$. This energy will disappear through diffusive damping. Therefore, the numerical scheme should satisfy

$$T_{b|v} = -T_{v|b} = D_M, \tag{2.11}$$

where

$$T_{b|v} \equiv \sum_{k=0}^{k_{max}} T_{b|v_k}(k), \tag{2.12}$$

$$T_{v|b} \equiv \sum_{k=0}^{k_{max}} T_{v|b_k}(k), \tag{2.13}$$

and k_{max} is the largest wave number in Fourier space and is equal to $N/2$. Fig. 2.1 shows that the code satisfies equation (2.11). The two curves $T_{b|v}(t)$ and $-T_{v|b}(t)$ coincide exactly. It is interesting to note that there is a time delay between $T_{b|v}$ $(= T_{v|b})$ and D_M, which is a measure of the energy cascade time.

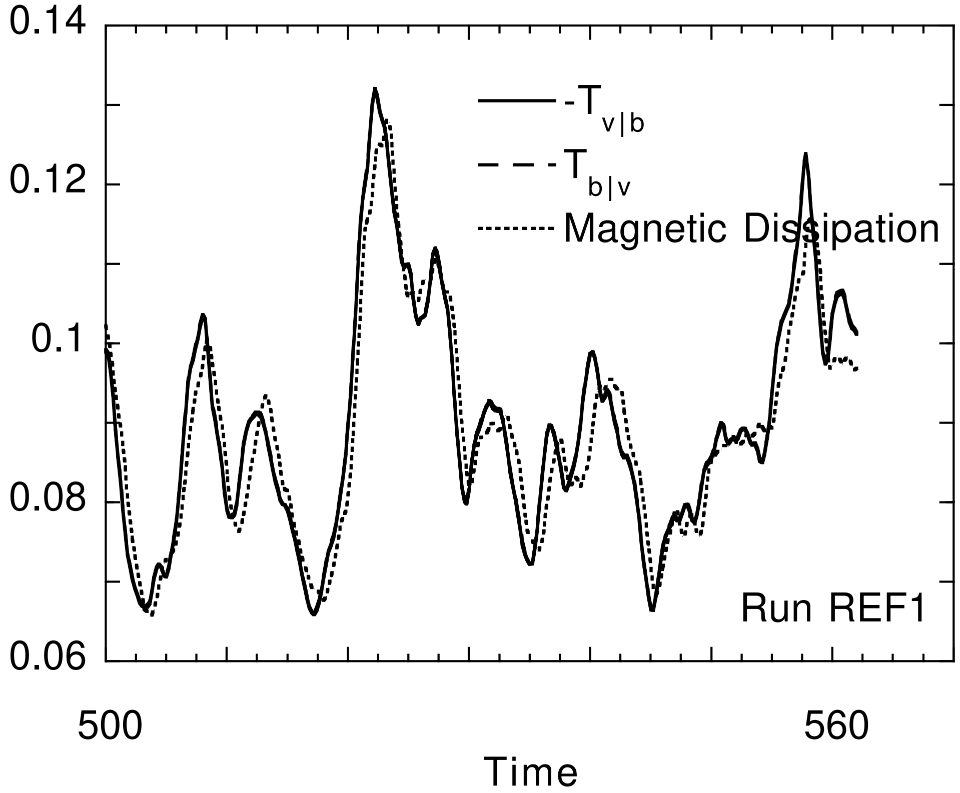

Figure 2.1: Test of the code. Time evolution of $T_{b|v}$, $-T_{v|b}$, and magnetic dissipation. $T_{b|v}$ and $-T_{v|b}$ coincide exactly. Magnetic dissipation shows a time delay, which is the turbulent diffusion time scale. Run REF1 (see Table 4.1).

Chapter 3

Strong External Magnetic Field Cases

3.1 Introduction

Many astrophysical plasmas, including the interstellar medium and the solar wind, often show magnetic fields whose energy density is greater than or equal to the local kinetic energy energy. In these plasmas the magnetic fields play a dominant dynamical role, mediated by magnetohydrodynamic (MHD) waves. In the incompressible limit, there are only two types of linear modes: shear Alfvén waves and pseudo Alfvén waves. While these two modes have different polarization directions, they have the same dispersion relation and propagate along the magnetic field lines at the Alfvén speed. Therefore, the nonlinear interactions of wave packets moving along the magnetic field lines at the Alfvén speed determine the dynamics of incompressible magnetized plasmas with a strong background field. In this paper, we study the anisotropy of the MHD turbulence in this regime. We will refer to this turbulence as incompressible Alfvénic turbulence.

Nonlinear processes and the corresponding energy spectrum of incompressible Alfvénic turbulence are still among the most controversial problems in

MHD. Since the pioneering works of Iroshnikov (1963) and Kraichnan (1965), the Iroshnikov-Kraichnan (IK) theory has been widely accepted as a model for incompressible, highly conducting MHD turbulence. The IK theory predicts $E_M(k) \sim E_K(k) \sim k^{-3/2}$ from a Kolmogorov-like dimensional analysis. Here, $E_M(k)$ and $E_K(k)$ are the magnetic and kinetic energy spectra respectively. In this framework, two counter-traveling eddies (i.e. Alfvén wave packets) interact and transfer energy to smaller spatial scales only when they collide, as they move in opposite directions along the magnetic field lines. Since the duration of such a collision is shorter than the conventional eddy turnover time by a factor of $t_v(l)/t_A(l)$, this collisional process is inefficient and the spectral energy transfer time as a function of scale l $(= t_{cas}(l))$ increases by the same factor compared to the eddy turnover time (l/v_l) in ordinary hydrodynamic turbulence. Here $t_v(l) = l/v_l$ and $t_A(l) = l/V_A$ are eddy turnover time and Alfvén time respectively, $V_A \equiv B/\sqrt{4\pi\rho}$, and B is rms magnetic field strength. When the external field is strong, as assumed in IK theory, this quantity is usually set to B_0, the strength of the uniform background field. If the spectral energy cascade rate

$$\epsilon \sim \frac{v_l^2}{t_{cas}(l)} \sim \frac{v_l^3}{l}\frac{t_A(l)}{t_v(l)} \tag{3.1}$$

is scale-independent and $E_M(k) \approx E_K(k)$, then we obtain the IK energy spectra.

The IK theory assumes an isotropic distribution of energy in $\mathbf{k}$-space. However, many researchers have argued that anisotropy is an important characteristic in MHD turbulence (for example, Shebalin et al. 1983; Montgomery and Matthaeus 1995). This anisotropy results from the resonant conditions for 3-wave interactions (or 4-wave interactions, when 3-wave interactions are null). The resonant conditions for the 3-wave interactions are

$$\mathbf{k}_1 + \mathbf{k}_2 = \mathbf{k}_3, \tag{3.2}$$

$$\omega_1 + \omega_2 = \omega_3, \tag{3.3}$$

where $\mathbf{k}$'s are wavevectors and ω's are wave frequencies. The first condition can be viewed as momentum conservation and the second as energy conservation. Alfvén waves satisfy the dispersion relation: $\omega = V_A|k_{\|}|$, where $k_{\|}$ is the component of wavevector parallel to the background magnetic field. Since only opposite-traveling wave packets interact, $\mathbf{k}_1$ and $\mathbf{k}_2$ must have opposite signs. Then from equations (3.2) and (3.3), either $k_{\|,1}$ or $k_{\|,2}$ must be equal to 0. That is, zero frequency modes are essential for energy transfer. If $k_{\|,2} = 0$, we have

$$k_{\|,1} = k_{\|,3}, \tag{3.4}$$

$$k_{\|,2} = 0 \tag{3.5}$$

(Shebalin et al. 1983). Therefore, in the wavevector space, 3-wave interactions make energy cascade in directions perpendicular to the mean magnetic field. Since the energy cascade is strictly perpendicular to the mean magnetic field, the actives modes in wavevector space have a slab-like geometry with a constant width. The implication is that the nonlinear cascade of energy works against isotropy in $\mathbf{k}$ space. Furthermore, it is important to note that equations (3.2) and (3.3) are true only when wave amplitudes are constant. In reality, nonlinear interactions provide a natural broadening mechanism, following the uncertainty relation, $\Delta t \cdot \Delta\omega \sim 1$. In particular, if a wave has a frequency less than or comparable to the nonlinear interaction rate, it is effectively a zero frequency mode.

Goldreich and Sridhar (1995, 1997) showed that in the strong incompressible shear Alfvénic turbulence regime (i.e. $\tau_{NL}^{-1} \sim \omega$), these arguments lead to a new scaling law with a scale-dependent anisotropy. In this model smaller eddies are more elongated. Their arguments are based on the assumption of a *critically balanced* cascade, $k_{\|}V_A \sim k_{\perp}v_l$, where $k_{\perp}$ and $k_{\|}$ are wave numbers perpendicular and parallel to the external dc field[1]. The argument given above for 3-wave interactions makes it clear that $k_{\perp}$ will tend to increase until it becomes important in the plasma dynamics. The assumption of strong nonlinearity implies that wave packets lose their identity after they travel one wavelength along the field lines. Consequently the eddy turnover time $((k_{\perp}v_l)^{-1})$ is actually the same as Alfvénic time $((k_{\|}V_A)^{-1})$. In this model, the cascade time, $t_{cas}(l)$ can be determined without ambiguity: $t_{cas} \approx (k_{\perp}v_l)^{-1} \approx (k_{\|}V_A)^{-1}$. Since the cascade time is comparable to the period of Alfvén wave, the 3-wave resonant condition can be violated according to the uncertainty relation $\Delta\omega \cdot \Delta t \sim V_A k_{\|} \cdot t_{cas} \sim 1$. The quantity $k_{\|}$ is the width of the active region in wavevector space. Finally the assumption of a scale-independent cascade rate

[1]Later in this Chapter, we will use $\tilde{k}_{\perp}$ and $\tilde{k}_{\|}$, instead of $k_{\perp}$ and $k_{\|}$, to represent their scaling relation in a slightly different, yet we believe equivalent, viewpoint. Here, $\tilde{k}_{\perp}$ and $\tilde{k}_{\|}$ are wavenumbers with respect to the direction of the local magnetic field, not the external field.

$\epsilon \sim v_l^2/t_{cas}(l) \sim E_{waves}V_A/L$ gives

$$k_{\|} \sim k_\perp^{2/3} L^{-1/3} \left(\frac{E_{waves}}{V_A^2}\right)^{1/3}, \tag{3.6}$$

$$v_l \sim V_A(k_\perp L)^{-1/3} \left(\frac{E_{waves}}{V_A^2}\right)^{1/3}, \tag{3.7}$$

where E_{waves} is the wave energy per mass. These formulae assume that all scales, from L on down, are within the inertial range of MHD turbulence. Here the typical $k_{\|}$ should be interpreted as the size of the range of parallel wavevectors, corresponding to a given $k_\perp$, that contain significant energy.

Matthaeus et al. (1998) recently tested this model numerically, and showed that the anisotropy of low frequency MHD turbulence scales linearly with the ratio of perturbed and total magnetic field strength (b/B), a result which seems inconsistent with Goldreich and Sridhar's model. To explain this scaling relation, they suggested that the region of Fourier space where the energy transfer takes place actively is given by

$$|\mathbf{k} \cdot \frac{\mathbf{B}_0}{\sqrt{4\pi\rho}}| < \frac{1}{\tau_{NL}}, \tag{3.8}$$

where τ_{NL} is the eddy turnover time of the energy containing length L. Consequently, "the region of the wave number space where spectral transfer is most vigorous" has a slab-like geometry with a constant width proportional to $1/(\tau_{NL}B_0)$.

All these theories (except the IK theory) share a common prediction for anisotropy: anisotropy should be more pronounced on smaller scales. Oughton et al. (1994) and Ghosh and Goldstein (1997) already reported this scale-dependent anisotropy through numerical simulations. The former extended Shebalin et al. (1983)'s 2-D calculations to 3-D cases. To measure anisotropy, they introduced the Shebalin angles, θ_Q, defined by

$$\tan^2\theta_Q = (\sum k_\perp^2 |\mathbf{Q}(\mathbf{k},t)|^2)/(\sum k_\parallel^2 |\mathbf{Q}(\mathbf{k},t)|^2),$$

where $\mathbf{Q}$ is vector potential $\mathbf{A}$, magnetic field $\mathbf{B}$, or current $\mathbf{J}$, etc. Greater θ_Q means greater anisotropy. They found that $\theta_A < \theta_B < \theta_J$. If the energy spectrum of $\mathbf{B}$ scales as $E_M(k) \propto k^{-s}$, then the spectra of vector potential and current scale as $E_A(k) \propto k^{-s-2}$ and $E_J(k) \propto k^{-s+2}$, respectively. The spectra of vector potential has the steepest slope among the three spectra. This means that the vector potential is least strongly dependent on small scales (and the current is most strongly dependent on small scales). Therefore they concluded that anisotropies are more pronounced at smaller scales[2]. They also found

[2]The width of the active region in Fourier space, $k_\parallel$, is a function of $k_\perp$. If

$$\left[\frac{k_\parallel}{k_\perp}\right]_{\text{small } k_\perp} > \left[\frac{k_\parallel}{k_\perp}\right]_{\text{large } k_\perp},$$

then we will have the ordering of Shebalin angles as observed by Shebalin et al. and Oughton et al. However, if $k_\parallel \propto k_\perp$, then we do not expect any ordering among the angles. In §3, we will find that, no matter what the true functional form $k_\parallel = k_\parallel(k_\perp)$ is, Fourier transformation smooths out the *true* relation and leads to a *fake* linear relationship between $k_\parallel$ and $k_\perp$. This suggests that their results are in contradiction to our discussion in §3. However, the apparent linear relationship between $k_\parallel$ and $k_\perp$ in §3 is not perfectly linear. Instead, we expect $k_\parallel = c_1 k_\perp + c_2$, where c_1 is a decreasing function of B_0 and c_2 depends on the $k_\parallel$ of forcing terms (or initial values of $k_\parallel$ for decaying turbulence). The presence of c_2 does not seem to be important in our Fig. 3 in §3. However, it does affect the calculation of Shebalin angles. That is, because of c_2, the ratio $k_\parallel/k_\perp = c_1 + c_2/k_\perp$ becomes a function of $k_\perp$. At the largest energy containing eddy scale, $k_\perp \sim c_2$ and hence $k_\parallel/k_\perp \sim c_1 + O(1) \sim O(1)$. But, at small scales, the ratio can be much smaller than unity. Therefore, because of c_2, we can obtain a scale-dependent anisotropy: $(k_\parallel/k_\perp)$ at small $k_\perp$ is greater than that at large a similar ordering for velocity field (and vorticity, etc). On the other hand, Ghosh and Goldstein (1997) calculated the Shebalin angles as a function of wavenumber bin. They found that the Hall-MHD[3] simulations show increased anisotropy at small scales (i.e. greater Shebalin angles at smaller scales). However their standard MHD simulations do not show increased anisotropies at small scales. We refrain from comparing their work with ours because they used different physics (the Hall effect) and their simulations are 2 1/2 dimensional. The simulations given in this paper are 3-D standard MHD simulations. We note that none of the previous papers quantitatively compared their results with particular theories of anisotropy.

In this Chapter, we examine the scaling law for Alfvénic MHD turbulence numerically and resolve the controversy concerning the anisotropic structure of the turbulence. Our results are consistent with Goldreich and Sridhar's model. We general results in §3.2. In §3.3, we describe our results for anisotropy in wavevector space. In this section, we demonstrate that none of the scaling laws mentioned above agrees with our data, and explain why a straightforward evaluation of the distribution of spectral power does not correspond to a physically meaningful set of scaling laws. We attribute this to the systematic

---

$k_\perp$. Note that this is a result of the initial conditions, rather than a true scaling relation. This will lead the ordering of the angles as observed by Shebalin et al. and Oughton et al.. This interpretation is qualitatively consistent with their results. For example. the ratio $k_\parallel/k_\perp = c_1 + c_2/k_\perp^{peak}$, therefore $(\tan\theta_Q)^{-1}$, approaches to a constant value $c_2/k_\perp^{peak}$ as B_0 becomes strong. Here $k_\perp^{peak}$ is the wavenumber of the peak of the energy spectrum. It is also possible to explain the increased anisotropy at high magnetic Reynolds numbers. If the magnetic Reynolds number increases, then $k_\perp^{peak}$ increases and, therefore, the ratio decreases.

[3]Hall MHD includes the Hall term, which is important at ion-cyclotron scales. In this paper, we consider only the standard MHD equations.

effects of large scale curvature of the magnetic fields. In §3.4, we determine the shape of individual eddies, avoiding the systematic error described above. We compare our results to Goldreich and Sridhar's model and give our conclusions in §3.5.

3.2 General Results

We list parameters used for the simulations in Table 3.1. We use the notation XY-Z, where X = 256 or 144 refers to the number of grids in each direction; Y = H or P refers to hyper- or physical viscosity; Z = $B_0 1$ or $B_0 0.5$ refers to the strength of the external magnetic fields.

Fig. 3.1 shows the evolution of V^2 and B^2 from Runs 256H-$B_0$1 and 144H-$B_0$1. Results of 256H-$B_0$1 are plotted as solid lines, and results of 144H-$B_0$1 are plotted as dotted lines. Both runs have similar results for the overlapped time, which means that the values of V^2 and B^2 are not sensitive to the spatial resolution. The magnetic energy density grows fast at the beginning of the simulations, as a result of the stretching of external field lines by turbulent motion. Since the external field is strong, magnetic forces soon become strong enough to balance the stretching effect. This balance happens at $t \sim 1$ and, after a transient stage ($1 \leq t \leq 5$), the turbulence reaches the saturation stage ($t \geq 5$). In this case the saturation stage begins quite early, since the external uniform magnetic field is strong and the magnetic diffusivity is effectively 0. In general, when the external field is weaker and/or magnetic diffusivity is larger, the saturation stage occurs later. At the saturation stage, $B^2 \sim 1.45$

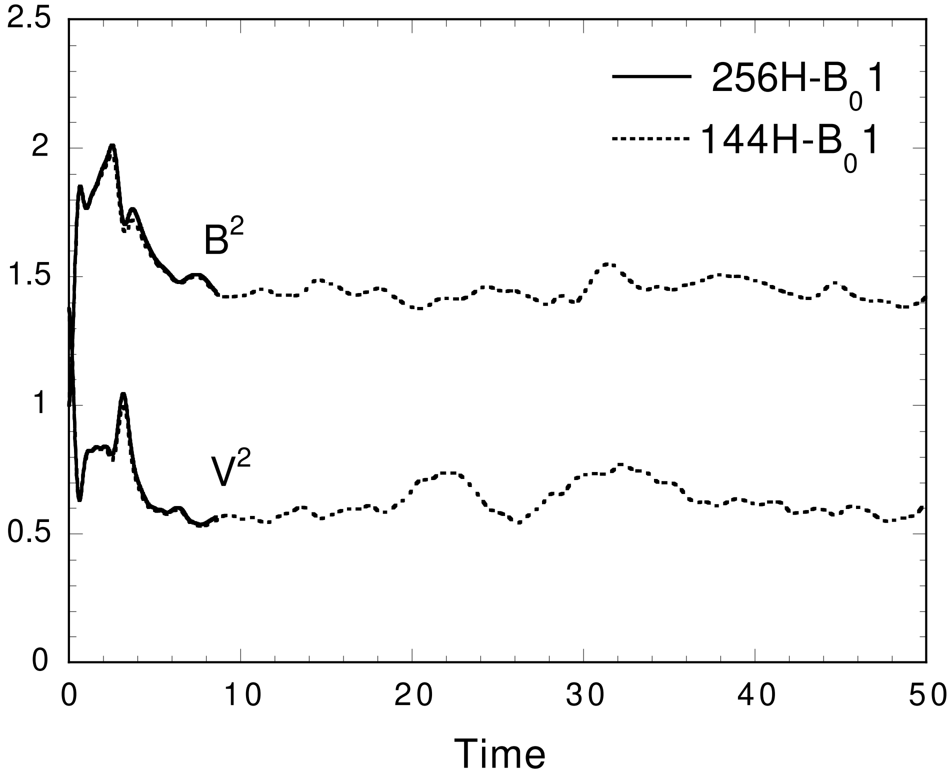

Figure 3.1: Time evolution of V^2 and B^2 (Solid lines, 256H-$B_0$1; Dotted lines, 144H-$B_0$1). $B_0 = 1$ for both Runs.

and $V^2 \sim 0.6$. Since $b^2 = B^2 - B_0^2(\equiv 1) \approx 0.45$, there is a rough energy equipartition between b and V. Note that, since $V \sim B$, the condition for strong MHD turbulence is met.

Run	N^3	ν	η	B_0
144H-$B_0$0.5	144^3	3.20×10^{-28}	3.20×10^{-28}	0.5
144H-$B_0$1	144^3	3.20×10^{-28}	3.20×10^{-28}	1
144H-$B_0$2	144^3	3.20×10^{-28}	3.20×10^{-28}	2
144H-$B_0$3	144^3	3.20×10^{-28}	3.20×10^{-28}	3
256H-$B_0$0.5	256^3	6.42×10^{-32}	6.42×10^{-32}	0.5
256H-$B_0$1	256^3	6.42×10^{-32}	6.42×10^{-32}	1
256P-$B_0$1	256^3	0.001	0.001	1

Table 3.1: Parameters

3.3 Fourier Analysis: A False Scaling Law?

3.3.1 Fourier Analysis

In this subsection, we investigate the spectral structure of Alfvénic turbulence. It is important to note that we lose some information about individual eddies when we perform a global transformation, such as the Fourier transformation. In particular, the scaling law given in this subsection may *not* be true for individual eddies (See §3.3.2 for details).

We plot the 1-dimensional energy spectra $E_K(k)$ and $E_M(k)$ in Fig. 3.2. Both spectra peak at the same k, which is also the scale of the energy injection. This reflects that there is a rough energy equipartition between b and V at the largest energy containing scale. In general, $E_K(k)$ always peaks at the energy

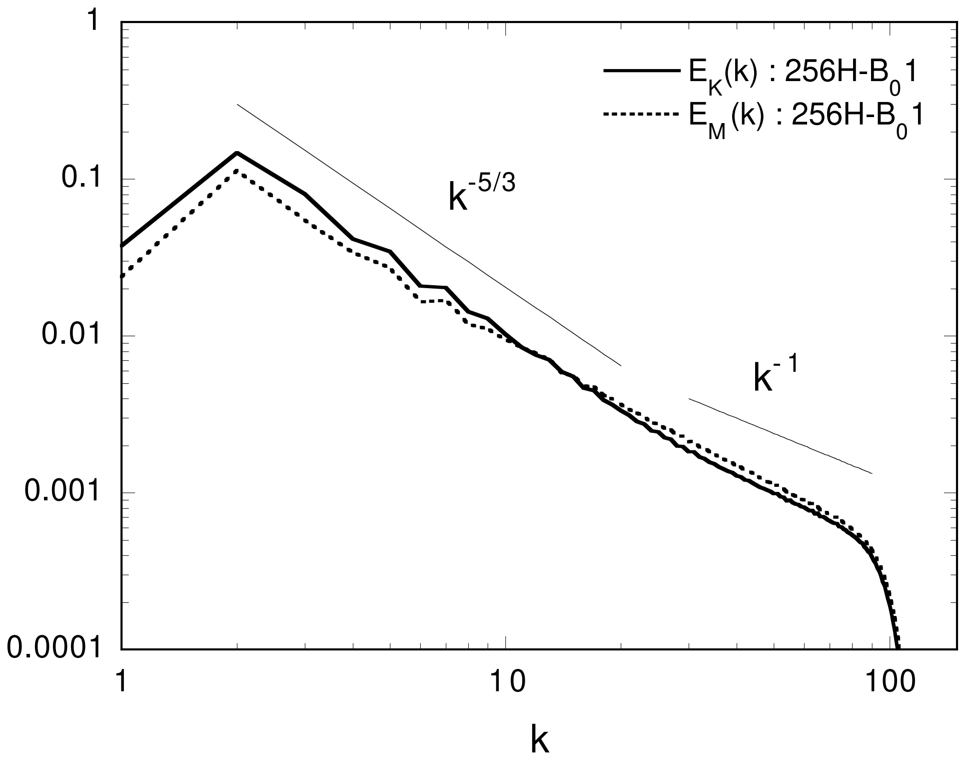

Figure 3.2: 256H-$B_0$1. Kinetic energy spectrum ($E_K(k)$) and magnetic energy spectrum ($E_M(k)$). For $2 \leq k \leq 20$, spectra are compatible with $k^{-5/3}$. A 1/k bottleneck effect is observed before the dissipation cutoff $k_d \sim 90$.

injection scale. However, $E_M(k)$ peaks at a larger k than $E_K(k)$ when the external field is weak. The inertial range exhibits two different scaling ranges: a small k range where the slopes are steep and a large k range where the slopes are mild. We believe that the former reflects a true inertial range, whereas the latter is a result of *bottleneck* effect. The $1/k$ bottleneck effect is a common feature in numerical hydrodynamic simulations with hyperviscosity (see Borue and Orzag 1996, 1995). Interestingly enough, the slope of the bottleneck is actually steeper than -1. This might mean that the bottleneck effect is less serious in MHD case. The kinetic and magnetic energy spectra have slightly different powers in the inertial range. Although the power indexes of both spectra are close to $-5/3$ in the (true) inertial range, the data are also compatible with IK theory, where the power index is $-3/2$.

We plot normalized 3-dimensional energy spectra of Run 256H-$B_0$1 in Fig. 3.3. In the figure, we plot contours of same

$$E_3(k_\perp, k_\|)/E_3(k_\perp, 0) \tag{3.9}$$

in $(k_\perp, k_\|)$ plane. As the energy cascades in the directions perpendicular to the mean field, this ratio drops as we move away from $k_\perp$ axis. The figure implies most of the energy is confined in a region around $k_\perp$ axis. The thickness of the region depends on the strength of the external magnetic fields (Fig. 3.4). We use the contours of $E_3(k_\perp, k_\|)/E_3(k_\perp, 0) = 0.5$ to measure the thickness. The angle $\Theta_{0.5}$ is the angle formed by the contours and the horizontal axis. We can see that $\tan\Theta_{0.5}$ $(= k_\|/k_\perp)$ is proportional to b/B_0. This result confirms the scaling relation found by Matthaeus et al. (1998). Both velocity and magnetic

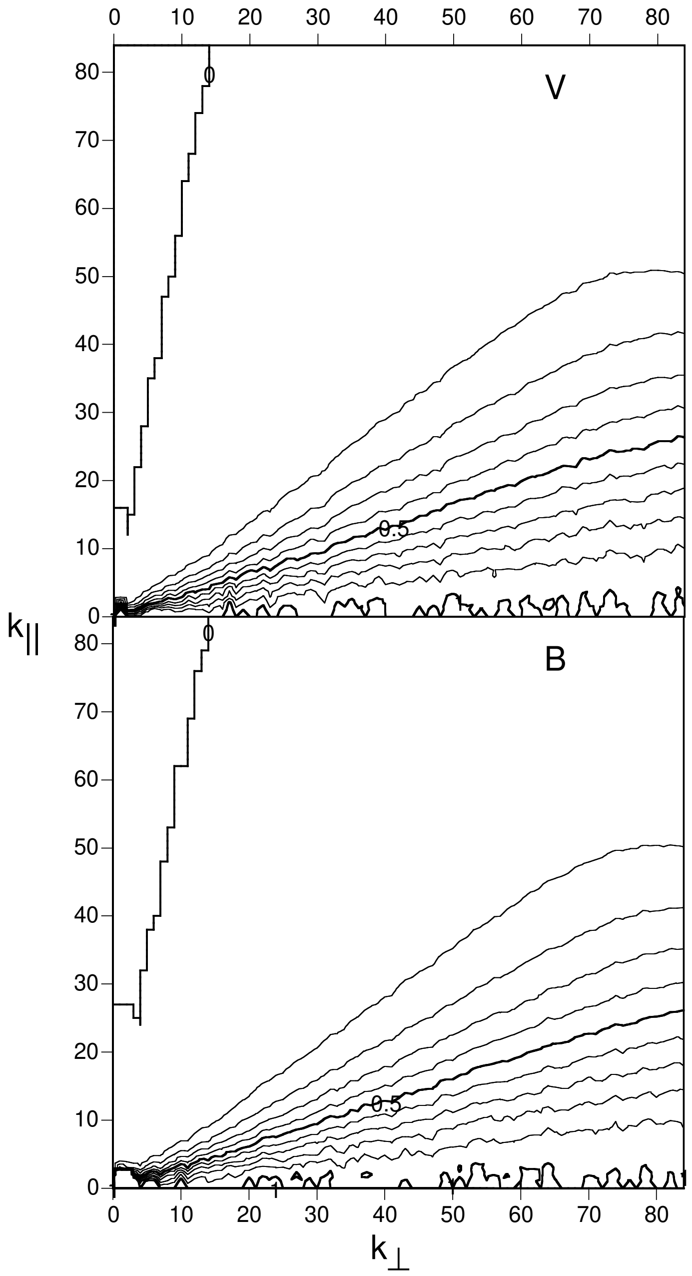

Figure 3.3: 256H-$B_0$1. 3D energy spectra normalized by the value on the $k_\perp$ axis.

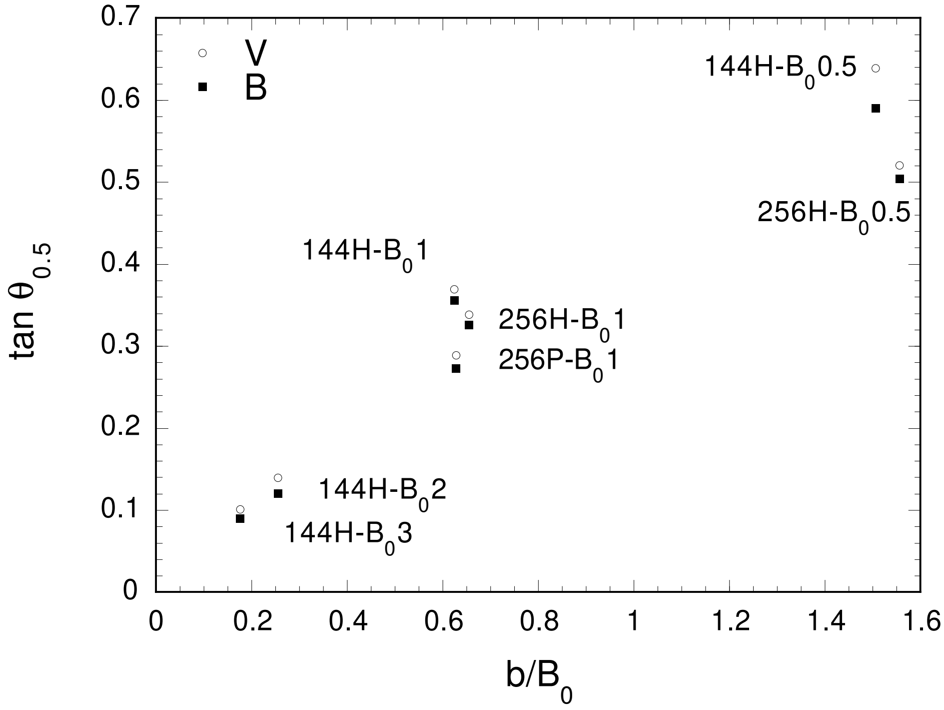

Figure 3.4: $\tan\Theta_{0.5}$ ($= k_{\|}/k_{\perp}$) versus b/B_0. These results are consistent with Matthaeus et al (1998) showing that anisotropy ($k_{\|}/k_{\perp}$) scales linearly with b/B_0.

fields have very similar structures. From the fact that $k_{\parallel} < k_{\perp}$ in the active region (see Fig. 3.3), one can conclude that eddies do have anisotropic structure: eddies are stretched along the direction of mean field. Apparently, Fig. 3.3 suggests that $k_{\parallel} \propto k_{\perp}$ and, hence, that anisotropy is scale-independent. No theory mentioned in §3.1 agrees with our result. However, it is not clear from the figure whether or not the true anisotropy is a function of scale: although contours show linear relationship between $k_{\parallel}$ and $k_{\perp}$, the relationship doesn't mean that all individual eddies have the same major axis to minor axis ratio. As explained in next subsection, the *rotation* of eddies by large-scale waves in the magnetic fields can distort the actual scaling relation and lead to the linear relationship shown in the figure.

Fig. 3.5 shows t_{phase} as a function of wavenumber k. This time scale is defined as the average correlation time Δt such that Fourier components at $\mathbf{k} = k$ have a phase shift of 60^o with respect to the original phase. We plot the result for zero frequency modes (i.e. $k_{\parallel}$=0 modes). We see that $t_{phase} \sim k^{-1}$ (that is, $k_{\perp}^{-1}$). How can we interpret this result? If a turbulent structure, characterized by a wavenumber k, moves a distance l then the phase is shifted by roughly kl, even if the eddy is unaffected by the motion. This implies that a large scale velocity V will change the phase at a rate kV, so that $t_{phase} \propto k^{-1}$. This implies that our calculation of t_{phase} is dominated by large scale motions rather than by the local cascade of energy, as long as the nonlinear cascade rate is proportional to k to some power less than one, which is generally the case. This is an example of how large-scale fluctuations can complicate attempts to

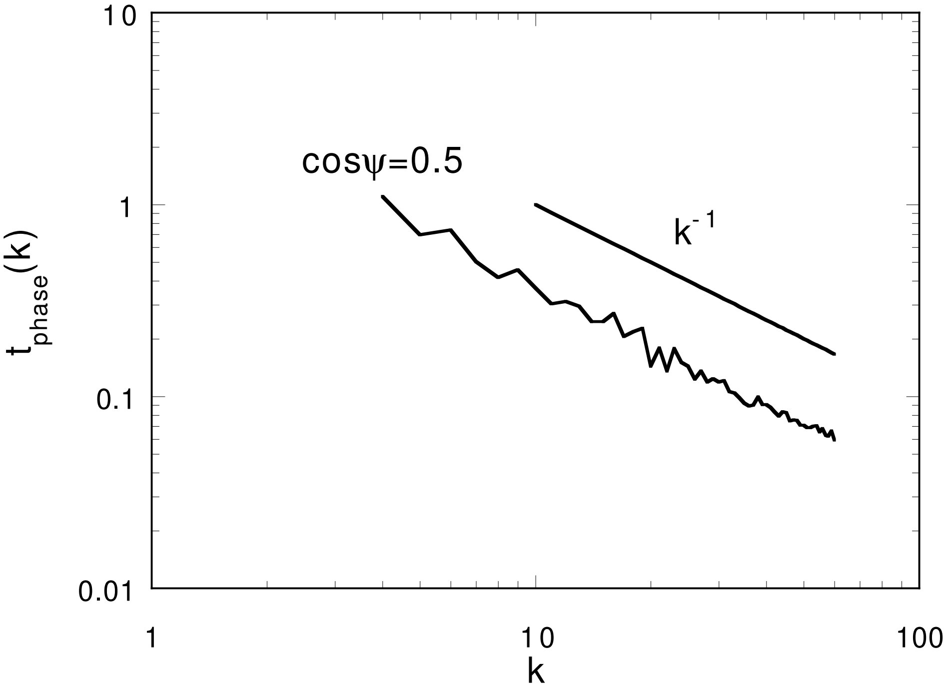

Figure 3.5: 256H-$B_0$1. Phase correlation time t_{phase} as a function of wavenumber, defined as the average time required for the phase to shift by 60^o.

find physically meaningful scaling relations.

3.3.2 Rotation Effect

In the previous subsection, we showed that anisotropy appears to be scale-independent. In this subsection, we will show that this apparent scaling relation is an artifact caused by the Fourier transformation. That is, we will demonstrate that large-scale modes in the magnetic field can distort the actual scaling law at smaller scales when we perform a Fourier transformation. In this manner, a straightforward evaluation of anisotropy in Fourier space is strongly contaminated by the curvature of the large-scale magnetic fields and does not reflect the actual local anisotropy when anisotropy is more pronounced at smaller scales. Consequently, figures 3.3 and 3.4 are compatible with any scaling law that predicts that smaller eddies are more elongated.

Fig. 3.3 implies that eddies have anisotropic shapes: on average, eddies are stretched along the direction of $\mathbf{B}_0$. However, not all eddies are aligned along the large scale field. The elongation of an eddy is determined by its interaction with the *local* magnetic field, not the background field. Since the large-scale magnetic field lines wander with respect to $\mathbf{B}_0$, all smaller scale eddies have similar angular distributions around $\mathbf{B}_0$. We illustrate this effect in Fig. 3.6.

In this way, we can explain the results of Goldreich and Sridhar (1995) and Matthaeus et al. (1998) simultaneously. Suppose that eddies are oriented according to the local field lines (Fig. 3.6a). Goldreich and Sridhar's result im-

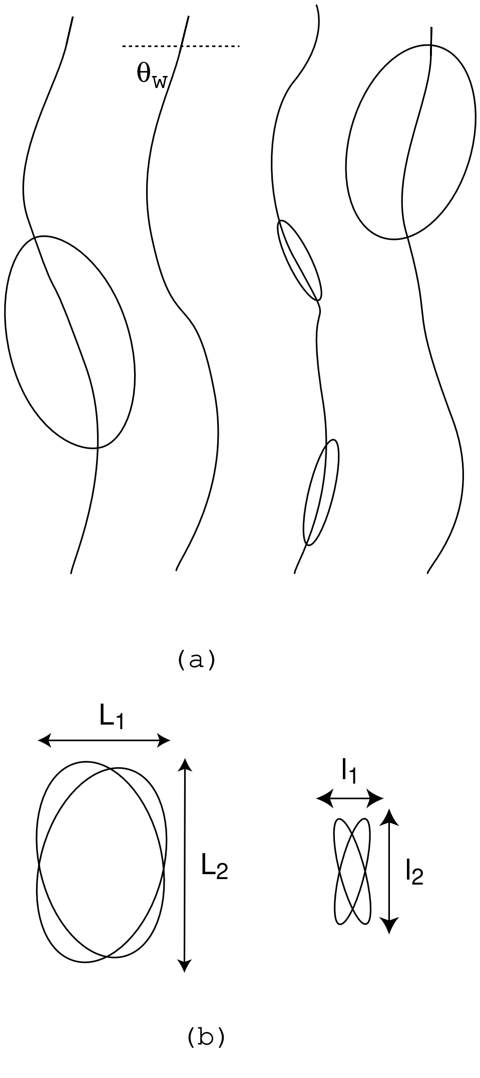

Figure 3.6: Rotation effect. (a) Anisotropic wave packets are moving along magnetic field lines. We assume the wave packets are aligned with the direction of local magnetic field lines. (b) Large scale variations in the magnetic field direction causes wave packets to point in different directions as a function of location. We expect $L_1/L_2 = l_1/l_2$. In Fourier space, L_1 (and l_1) become $\sim 1/k_\perp$ and L_2 (and l_2) becomes $\sim 1/k_\parallel$. Consequently, information about eddy shapes is lost when we look at the power spectrum.

plies smaller eddies are relatively more elongated. When we perform a Fourier transformation and measure the ratio of $k_{\|}/k_{\perp}$, what we actually measure is not the ratio of the minor axis to the major axis of individual eddies. Instead, because the direction of the local magnetic field varies according to location and Fourier transformation is none other than a (weighted) averaging process, we actually measure the ratio averaged over all possible orientation of the eddies (Fig. 3.6b). The Fourier transformation sees that L_1 (and l_1) is the minor axis and L_2 (and l_2) is the major axis of an eddy. The ratio of L_1/L_2 ($= l_1/l_2$) is determined by the degree of the *wandering* of the large scale magnetic field lines with respect to $\mathbf{B}_0$ and, therefore, the ratio is nearly constant for all eddies, regardless of their sizes and shapes. In fact, the ratio will depend on the tangent of the angle between $\mathbf{B}_0$ and $\mathbf{B}$. Since $k_{\perp} \propto 1/L_1$ and $k_{\|} \propto 1/L_2$, the *measured* value of the ratio $k_{\|}/k_{\perp}$ is nearly scale-independent. We expect the angle θ ($\equiv 90^o - \theta_w$) between $\mathbf{B}_0$ and $\mathbf{B}$ to be

$$\tan\theta = b/B_0. \tag{3.10}$$

Therefore, we have

$$\sin\theta = b/B = \cos\theta_w, \tag{3.11}$$

which is exactly the scaling relation found by Matthaeus et al.

3.4 Measuring Eddy Shapes

In this section, we analyze the shape of eddies in real space. As explained in the previous section, we assume that elongated eddies are aligned in the direction of the *local* magnetic fields. If we want to visualize the shape of eddies, we need to first identify the direction of the *local* magnetic fields. It is important to note that, although we use the term 'local magnetic fields' for simplicity, the fields are different from $\mathbf{B}(\mathbf{r})$. Let us consider an eddy of size l. The 'local magnetic field' of the eddy must act as the 'large-scale magnetic field' for the eddy. Therefore, the 'local magnetic fields' for eddies of size l, must be smoothly varying vector fields whose characteristic length of variation is $> l$. Note also that another eddy of size l' ($\neq l$) at the same location can have a slightly different direction for the 'local magnetic field.' The 'local magnetic fields' are functions of position ($\mathbf{r}$) and eddy size (l). Then, how can we define the direction of the *local* magnetic fields? We implement 2 independent numerical algorithms to calculate the direction of the *local* magnetic fields.

In the first method, the local magnetic fields are calculated by

$$\mathbf{B}_l = (\mathbf{B}(\mathbf{r}_1) + \mathbf{B}(\mathbf{r}_2))/2 \tag{3.12}$$

and the second order structure functions for v and b are given by

$$F_2^v(R, z) =< |\mathbf{V}(\mathbf{r}_1) - \mathbf{V}(\mathbf{r}_2)|^2 >, \tag{3.13}$$

$$F_2^b(R, z) =< |\mathbf{b}(\mathbf{r}_1) - \mathbf{b}(\mathbf{r}_2)|^2 >, \tag{3.14}$$

where $R = |\hat{\mathbf{z}} \times (\mathbf{r}_2 - \mathbf{r}_1)|$, $z = \hat{\mathbf{z}} \cdot (\mathbf{r}_2 - \mathbf{r}_1)$ and $\hat{\mathbf{z}} = \mathbf{B}_l/|\mathbf{B}_l|$. That is, R and z are coordinates in a cylindrical coordinate system in which the z-axis is parallel to $\mathbf{B}_l$ (Fig. 3.7). $\mathbf{B}(\mathbf{r})$ and $\mathbf{b}(\mathbf{r})$ are the total and perturbed magnetic fields at a point $\mathbf{r}$. As usual, brackets denotes a spatial average.

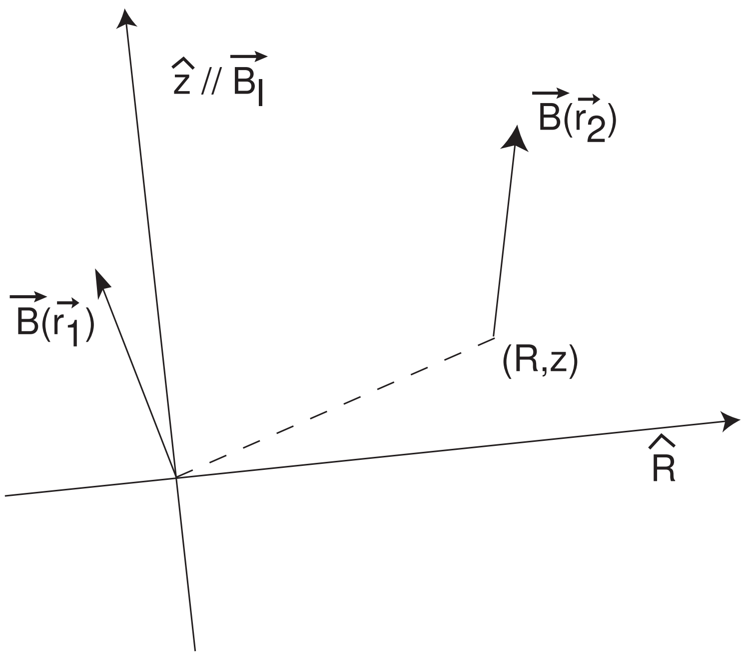

Figure 3.7: Method 1. We adopt a cylindrical coordinate system in which z-axis is parallel to $\mathbf{B}_l = (\mathbf{B}(\mathbf{r}_1) + \mathbf{B}(\mathbf{r}_2))/2$.

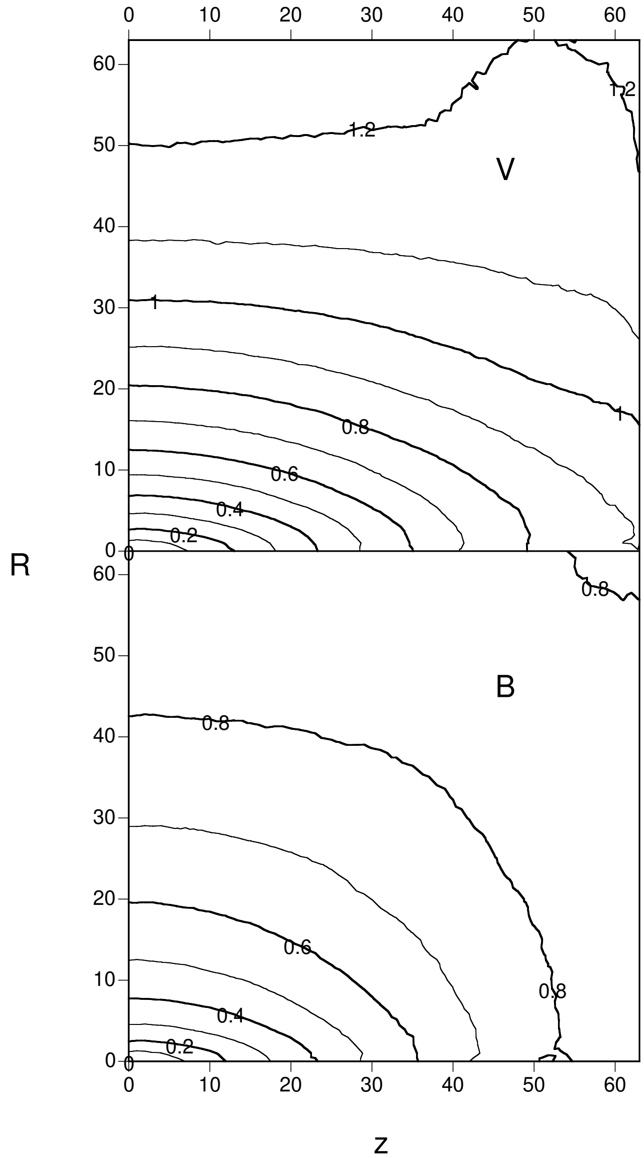

Figure 3.8: 256H-$B_0$1. Visualization of eddies using method 1. Note that horizontal axis is z-axis (see Fig. 3.7 for definition). Unit is grid spacing. Smaller eddies are more elongated.

In Fig. 3.8 we plot the second order structure functions in z-R plane. The horizon axis (z-axis) is parallel to $\mathbf{B}_l$. The contours reflect the shapes of the eddies. Eddies are clearly elongated along the local field lines, and smaller eddies are more elongated. The velocity and magnetic fields show different structure at large scales. However, their small scale structure is quite similar.

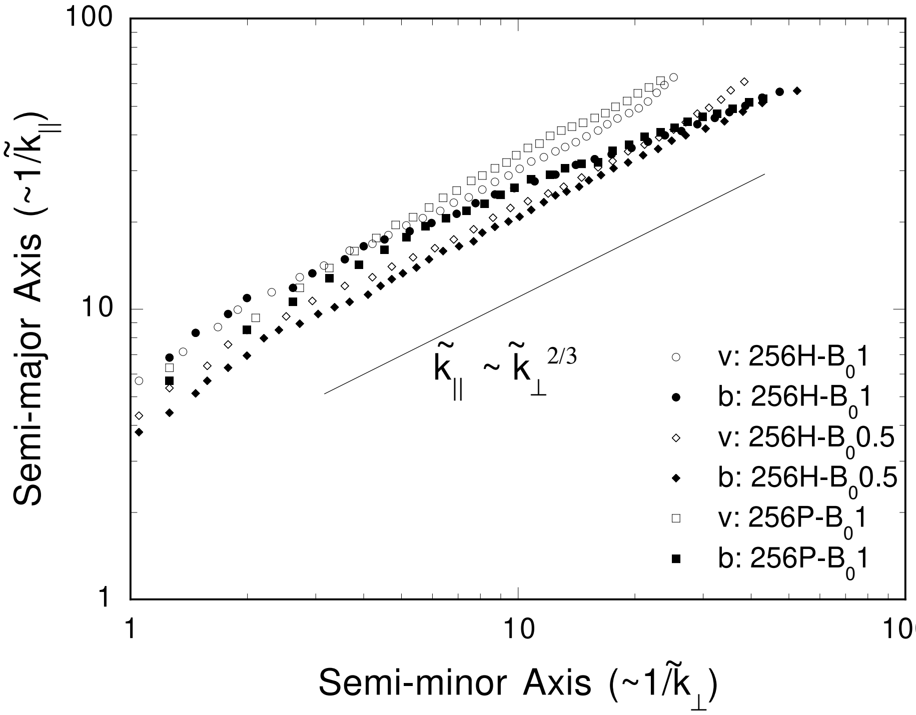

Figure 3.9: R-intercept (semi-minor axis; $\sim 1/\tilde{k}_\perp$) versus z-intercept (semi-major axis; $\sim 1/\tilde{k}_\parallel$) from Fig. 3.8. In 256H-$B_0$0.5, both velocity and magnetic fields follow the relation $\tilde{k}_\parallel \sim \tilde{k}_\perp^{2/3}$. In 256H-$B_0$1 and 256P-$B_0$1, velocity fields follow the same scaling relation. However, magnetic fields scale slightly differently.

In Fig. 3.9, we plot R-intercepts and z-intercepts of the contours. The

R-intercept and z-intercept of a given contour can be regarded as a measure of $\tilde{k}_\perp$ and $\tilde{k}_\|$ for the corresponding eddy scale[4]. Fitting the results for velocity fields gives

$$v : \tilde{k}_\| \sim \begin{cases} \tilde{k}_\perp^{0.69}, & (256H - B_0 0.5) \\ \tilde{k}_\perp^{0.70}, & (256H - B_0 1) \\ \tilde{k}_\perp^{0.73}, & (256P - B_0 1) \end{cases} \tag{3.15}$$

On the other hand, for the magnetic fields we find

$$b : \tilde{k}_\| \sim \begin{cases} \tilde{k}_\perp^{0.64}, & (256H - B_0 0.5) \\ \tilde{k}_\perp^{0.50}, & (256H - B_0 1) \\ \tilde{k}_\perp^{0.53}, & (256P - B_0 1) \end{cases} \tag{3.16}$$

The velocity fields show good agreement with the scaling relation, $\tilde{k}_\| \sim \tilde{k}_\perp^{2/3}$, proposed by Goldreich and Sridhar (1995). The power indices are insensitive to strength of B_0 or the form of viscosity (and diffusivity). However, the magnetic field shows different scaling behavior. When the external field is moderately strong (256H-$B_0$0.5), the power index is very close to 2/3. On the other hand, for stronger external fields (256H-$B_0$1 and 256P-$B_0$1), the power indices are smaller than 2/3. The results are insensitive to the choice of viscosity (and diffusivity). It is not clear whether the existence of a separate scaling law for the magnetic field represents a physical effect not included in Goldreich and Sridhar's model, e.g. the first signs of small scale intermittency in the magnetic field distribution, or merely the failure of the numerical models used here to fully resolve the inertial range of strong MHD turbulence.

---

[4]We interpret $\tilde{k}_\|$ as the inverse of the major axis of eddies and $\tilde{k}_\perp$ as that of the minor axis. Since the major axis is assumed to be parallel to the local magnetic fields, $\tilde{k}_\|$ is the parallel wavenumber with respect to the *local* magnetic field direction. On the other hand, in §3.3.1, $k_\|$ is parallel to $\mathbf{B}_0$. Therefore, $\tilde{k}_\|$ and $\tilde{k}_\perp$ in this section have different meaning from $k_\|$ and $k_\perp$ in §3.3.1.

In the second method, we employ a completely different approach. We obtain the local large scale magnetic fields by filtering out the small scale magnetic fields:

$$\mathbf{B}_\sigma(\mathbf{r}) = \sum_{\mathbf{r}'} \mathbf{B}(\mathbf{r}')\phi(|\mathbf{r} - \mathbf{r}'|), \tag{3.17}$$

where $\phi(r) \propto \exp(-r^2/\sigma_r^2)$ is a gaussian function. To determine the shape of small scale eddies (i.e. eddies smaller than the filter size, $\sim \sigma_r$), we consider the following quantities:

$$\mathbf{v}_\sigma(\mathbf{r}) = \mathbf{V}(\mathbf{r}) - \mathbf{V}_\sigma(\mathbf{r}), \tag{3.18}$$

$$\mathbf{b}_\sigma(\mathbf{r}) = \mathbf{B}(\mathbf{r}) - \mathbf{B}_\sigma(\mathbf{r}), \tag{3.19}$$

where $\mathbf{V}_\sigma$ and $\mathbf{B}_\sigma$ are filtered fields (cf. eq. (3.17)). The fields $\mathbf{v}_\sigma(\mathbf{r})$ and $\mathbf{b}_\sigma(\mathbf{r})$ represent small scale fluctuation of velocity and magnetic fields, the shape of which can be regarded as an adequate approximation of small scale eddies. From these two fields we calculate the structure functions

$$F^v(R, z) = |\mathbf{v}_\sigma(\mathbf{r}_2) - \mathbf{v}_\sigma(\mathbf{r}_1)|, \tag{3.20}$$

$$F^b(R, z) = |\mathbf{b}_\sigma(\mathbf{r}_2) - \mathbf{b}_\sigma(\mathbf{r}_1)|, \tag{3.21}$$

where R and z are similarly defined as in the first method with $\hat{\mathbf{z}} \parallel \mathbf{B}_\sigma(\mathbf{r}_1)$ (Fig. 3.10).

In Fig. 3.11, we plot the results of the second method. We can clearly observe the flattening effect: When the filter size is large, eddies are less anisotropic. When filter size is small, eddies show highly anisotropic structure. In the figure, we plot only the results for magnetic fields. Velocity fields

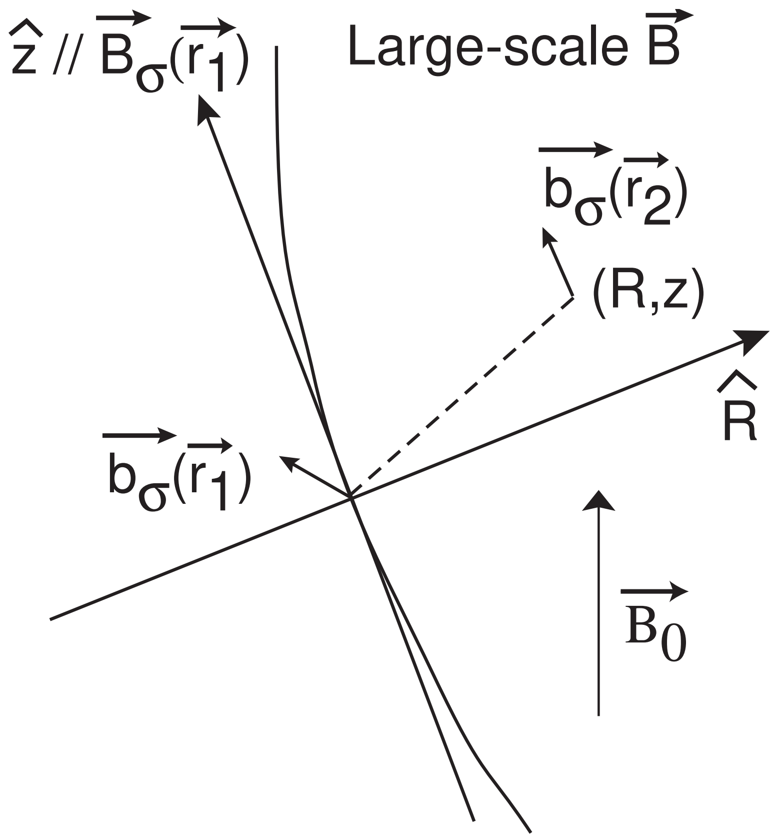

Figure 3.10: Method 2. We adopt a cylindrical coordinate system in which z-axis is parallel to large-scale fields $\mathbf{B}_\sigma$.

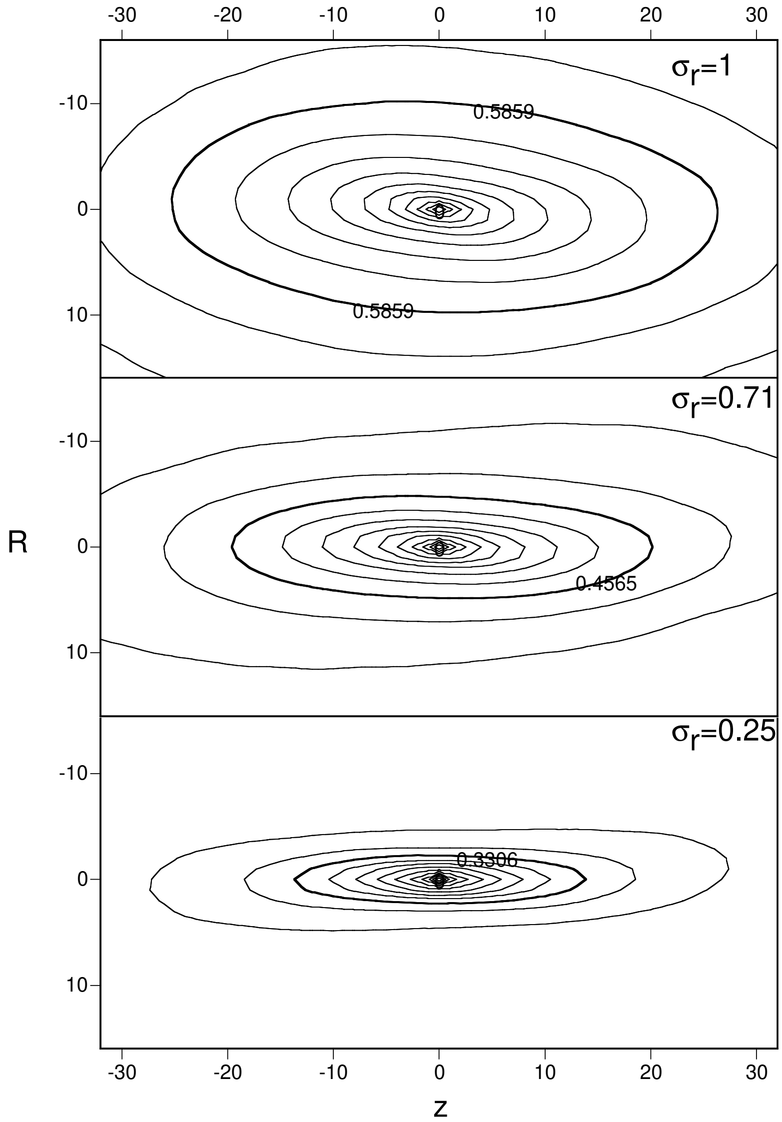

Figure 3.11: 256H-$B_0$1. Visualization of eddies using method 2. Note that horizontal axis is z-axis (see Fig. 3.10 for definition). Unit is grid spacing. Only magnetic fields are shown. Smaller eddies are more flattened.

show similar trends. The thick contours represent $F^b(R,z) =< |\mathbf{b}_\sigma|^2 >^{1/2}$. The values next to the thick contours are $< |\mathbf{b}_\sigma|^2 >^{1/2}$.

This second method is useful for visualizing small scale eddies, but may not be as useful for quantitative analysis. The difficulty comes from the fact that there is no well defined eddy scale associated with filtered fields $\mathbf{v}_\sigma(\mathbf{r})$ and $\mathbf{b}_\sigma(\mathbf{r})$.

In this paper, we will not pursue quantitative analysis using the method 2. Instead, we just wish to point out that both methods describe the same scaling law: smaller eddies are relatively more stretched along the local magnetic field lines. In particular, the results from the first method are consistent with the relation $\tilde{k}_\| \sim \tilde{k}_\perp^{2/3}$ proposed by Goldreich and Sridhar (1995).

3.5 Discussion and Conclusions

Here we rederive the scaling law $\tilde{k}_\| \propto \tilde{k}_\perp^{2/3}$ in the framework of 3-wave interactions. Except for the use of the uncertainty principle, the work in this section is independent of Goldreich and Sridhar's derivation. As noted by Goldreich and Sridhar (1995), 3-wave interactions are an adequate proxy for wave-wave interactions of all orders in a strong MHD turbulence. As long as we assume the locality of interactions, it is pointless to distinguish $k_\|$ and $k_\perp$ from $\tilde{k}_\|$ and $\tilde{k}_\perp$. Hence, for simplicity, we use $k_\|$ and $k_\perp$ instead of $\tilde{k}_\|$ and $\tilde{k}_\perp$ during the derivation.

Suppose the 3-dimensional energy spectrum is given by

$$E_3(k_\perp, k_{||}) \equiv |\hat{\mathbf{V}}(\mathbf{k})|^2 \propto k_\perp^{-2\alpha} f, \tag{3.22}$$

where $\hat{\mathbf{V}}(\mathbf{k})$ is the amplitude of the mode whose wavevector is $\mathbf{k}$ and $f(u)$ is a positive, symmetric function of u (cf. equation (7) of Goldreich and Sridhar (1995)) which describes the power distribution as a function of eddy shape. If the *width* (or, *thickness*) of the energy spectrum in the direction of $k_{||}$ is $k_\perp^\beta$, then we can write

$$E_3(k_\perp, k_{||}) \propto k_\perp^{-2\alpha} f(k_{||}/k_\perp^\beta). \tag{3.23}$$

If the *width* is caused by the uncertainty principle ($\Delta t{\cdot}\Delta\omega \approx 1$ with $\Delta t \propto t_{cas}(l)$ and $\Delta\omega \propto k_{||}$), then

$$t_{cas}(l) \propto k_\perp^{-\beta}. \tag{3.24}$$

Suppose the energy cascade rate $\epsilon \sim v_l^2/t_{cas}(l)$, where $l = 2\pi/k_\perp$, is scale-independent. Because $v_l^2 \sim k_\perp^{-2\alpha} k_\perp^2 k_\perp^\beta$ ($\sim k_\perp E(k_\perp)$, $E(k_\perp)$ = 1-dimensional spectrum) and $t_{cas}(l) \sim k_\perp^{-\beta}$, we have

$$k_\perp^{-2\alpha+2+2\beta} = const. \tag{3.25}$$

Therefore,

$$1 - \alpha + \beta = 0. \tag{3.26}$$

Now, let's pick up a mode at a wavevector $\mathbf{p}$ and consider nonlinear interactions with other wave modes. First, the strength of the interaction with another mode at $\mathbf{q}$ is $\propto p|\hat{\mathbf{V}}(\mathbf{p})||\hat{\mathbf{V}}(\mathbf{q})|$. (This comes from the $(\nabla \times \mathbf{V}) \times \mathbf{V}$ term in equation (2.1)) Hereafter we assume $p \equiv |\mathbf{p}| \approx p_\perp$. Second, the number of interactions is $\propto p^2 p^\beta$. This is the number of modes *near* $\mathbf{p}$. Here we use locality of 3-wave interactions. If the interactions are random, the net change of amplitude per unit time will be the strength of the interaction times the square root of the number of interactions, or

$$|\Delta \hat{\mathbf{V}}(\mathbf{p})| \propto p |\hat{\mathbf{V}}(\mathbf{p})| |\hat{\mathbf{V}}(\mathbf{q})| \cdot (p^2 p^\beta)^{1/2}. \tag{3.27}$$

Therefore, we have

$$t_{cas} \propto |\hat{\mathbf{V}}(\mathbf{p})| / |\Delta \hat{\mathbf{V}}(\mathbf{p})| \propto p^{-2} p^{\alpha} p^{-\beta/2}, \tag{3.28}$$

where we assumed $p \propto q$. Equating this with $t_{cas} \propto p^{-\beta}$, we can write

$$\alpha - 2 = -\beta/2. \tag{3.29}$$

From equations (3.26) and (3.29), we have

$$\alpha = 5/3, \beta = 2/3, \tag{3.30}$$

which is just the result of Goldreich and Sridhar (1995):

$$k_{\|} \propto k_{\perp}^{2/3}. \tag{3.31}$$

As a consequence, the 3-D energy spectrum becomes

$$E_3(k_\perp, k_\|) \propto k_\perp^{-10/3} f(k_\| / k_\perp^{2/3}) \tag{3.32}$$

and the corresponding 1-D spectrum is given by

$$E(k) \propto k^{-5/3}. \tag{3.33}$$

In summary, we have shown that the anisotropy of Alfvénic turbulence depends on the spatial scales of eddies. In particular, our results confirm the claim by Goldreich and Sridhar (1995, 1997) that smaller eddies are relatively more elongated along the direction of the local magnetic field lines than larger ones. Quantitative measurements of the anisotropy using the velocity fields show good agreement with their proposed scaling law, $k_{\|} \sim k_{\perp}^{2/3}$ as long we interpret these wavenumbers as referring to the *local* magnetic field direction. However, when the external magnetic field is very strong, magnetic fields scale somewhat differently, showing a slightly more rapid increase in anisotropy at smaller scales.

It is important to note that the correct scaling laws depend on comparing the eddy shape to the *local* magnetic field direction.

As a final note, we wish to stress that our results are not in agreement with the IK theory. The IK theory is based on the assumption of isotropy in wavenumber space, which may be true when the external magnetic field is very weak or zero. However, even in these cases, the turbulence is globally isotropic, but locally very anisotropic. In this paper, we showed that eddies do show anisotropy and that the anisotropy is scale-dependent when there is a strong large scale field (which should apply to very small scales within any MHD turbulence cascade). On the other hand, our results are consistent with Goldreich and Sridhar's theory of strong MHD turbulence. More precisely, if we consider the ratio of hydrodynamic to Alfvénic rates, that is $(kv_k/\tilde{k}_{\|}V_A)$, we find from equations (3.15) and (3.16) that

$$\frac{kv_k}{\tilde{k}_{\|}V_A} \propto \tilde{k}_{\perp}^{0.3-0.5} v_k, \tag{3.34}$$

where $k \approx \tilde{k}_{\perp}$. From Fig. 3.2 we see that for the inertial range this implies a ratio which is either constant or increasing with wavenumber. A constant ratio is predicted by Goldreich and Sridhar's model. The IK model predicts a slow decline.

Chapter 4

Weak External Magnetic Field Limits

4.1 Introduction

There are at least two distinct types of magnetohydrodynamic (MHD) turbulence. When the external large scale magnetic field is strong, the resulting turbulence can be described as the nonlinear interactions of Alfvén waves (e.g., Goldreich and Sridhar 1995, 1997). In contrast, when the external field is weak, MHD turbulence near the scale of the largest energy containing eddies will be more or less like ordinary hydrodynamic turbulence with a small magnetic back reaction. In this regime, the turbulent eddy turnover time at the large scale (L/V) is less than the Alfvénic time of the scale (L/B), where V and B are r.m.s. velocity and magnetic field strength (divided by $(4\pi\rho)^{1/2}$) respectively and L is the scale of energy injection or the largest energy containing eddies.

Various aspects of weak/zero external field MHD turbulence have been studied both theoretically and numerically. One of the most important issues in this regime is the generation of large scale fields. Since large scale magnetic fields are observed in almost all astrophysical objects, the generation and maintenance of such fields is of great importance. In mean field dynamo theory (see Moffatt 1978; Parker 1979), turbulent motions at small scales are biased to create a non-zero electromotive force along the direction of the large-scale magnetic field. This effect (the 'α-effect') works to amplify and maintain large-scale magnetic fields. Whether or not this effect actually works depends depends on the structure of the MHD turbulence, especially on the mobility of the field lines. For example, Vainshtein and Cattaneo (1992) have argued that when equipartition between magnetic and kinetic energy densities occurs at any scale larger than the dissipation scale, the mobility of the field lines and the α effect will be greatly reduced. An alternative approach, which may avoid such difficulties, is to appeal to small scale field line stretching alone to generate strong magnetic fields (Batchelor 1950; Kazantsev 1967). In this model large scale magnetic fields are actually composed of parallel fibrils of random polarity, i.e. the large scale field is defined by the preferred axis of the magnetic field direction, but there is little large scale flux in such fields. Whether or not the mean field dynamo mechanism works, it is interesting to contemplate whether or not such fine-grained fields can be produced in the absence of any α effect.

In addition, there are at least two other points of contention regarding the nature of magnetic fields generated in MHD turbulence. First, the mobility of magnetic fields will be affected by their intermittency. Various models for the generation and dynamics of flux tubes have been proposed, motivated in part by observations of the solar photosphere (e.g., Vishniac 1995a, 1995b; Brandenburg at al. 1995). However, so far numerical simulations have tended to show only modest levels of intermittency. Second, there is the nature of the energy cascade and power spectrum of MHD turbulence. There are numerous analytical models for dealing with MHD turbulence: the eddy-damped quasinormal Markovian (EDQNM) approximation (Pouquet et al. 1976), the renormalization group technique (Fournier at al. 1982), and others, including recent work by Goldreich and Sridhar (1995, 1997) in which they treated nonlinear eddy interactions as a series of interactions between marginally nonlinear Alfvén waves. The last is perhaps the most promising. The energy spectra of the MHD turbulence is one of the most poorly understood fields in astrophysics. Early work by Iroshnikov (1963) and Kraichnan (1965) obtained a $k^{-3/2}$ spectrum for both magnetic energy and kinetic energy in the presence of a dynamically significant magnetic field. However, this work was based on assumption of isotropy in wavenumber space, which is difficult to justify unless the magnetic field is very weak. Goldreich and Sridhar's model assumes a critical level of anisotropy, such that magnetic and hydrodynamic forces are comparable, and predicts a $k^{-5/3}$ spectrum for strong external field turbulence (which should apply to very small scales within any MHD turbulent cascade). Solar wind observations, which are well within the strongly magnetized regime, show an energy spectrum $E(k) \sim k^{-1.70}$ (Leamon et al. 1998). Numerical studies have only recently been able to address this question. Recent work by Cho and Vishniac (2000; see also Chapter 3) and Maron and Goldreich (1999) seems to support the scaling laws of Goldreich and Sridhar.

Here we will concentrate on the structure of magnetic fields in MHD turbulence when the external field is weak. In the case of hydrodynamical turbulence, the energy cascades to smaller scales. If we introduce a weak uniform magnetic field, turbulent motions will stretch the magnetic field lines and divert energy to the small scale magnetic field. As the magnetic field lines are stretched, the magnetic energy density increases rapidly, until the generation of small-scale magnetic structures is balanced by the magnetic back reaction at some scale between L and the dissipation scale. This will happen when the magnetic and kinetic energy densities associated with a scale l are comparable so that Lorentz forces resist further stretching at or below that scale[1]. However, stretching at scales larger than l is still possible, and the magnetic energy density will continue to grow if l can increase[2]. Eventually, a final stationary state will be reached.

This discussion raises two questions. What is the scale of energy energy equipartition? What is the magnetic field structure on this scale? The answer to the latter question will depend on the nature of diffusive processes acting on the magnetic field. First, suppose that magnetic field lines are unable to smooth the tangled fields at small scales. Then, as a result of the turbulent energy cascade and the subsequent stretching of magnetic field lines, magnetic fields have thin fibril structures with many polarity reversals within the energy equipartition scale l. Consequently, magnetic structures on the equipartition scale are highly elongated along the local magnetic field direction. This is the kind of picture one obtains by considering passive advection of magnetic fields

[1] The first energy equipartition scale l can be larger than the dissipation scale when the equipartition occurs before the energy cascade reaches the dissipation scale.

[2] Our results show that l does increase and the magnetic energy continues to grow.

in a chaotic flow (for a review, see Ott 1998). The degree to which this can be applied to a realistic, highly conducting fluid is controversial. On the other hand, if we assume MHD turbulence is always capable of relaxing tangled field lines at small scales, then we expect eddies at the final equipartition scale to be nearly isotropic. That is, the typical radius of curvature of field lines will be comparable to the scale of field reversal. This picture does not imply a clear expectation for the scale of equipartition in the stationary state. As we will see later, our simulations support the latter picture but with the energy equipartition scale near, but somewhat smaller than, the largest energy containing eddy scale.

In this Chapter, we will interpret the results of numerical simulations of MHD turbulence with a weak external field in terms of these models. In §4.2, we give general results. In §4.3, we present the main results of simulations. Finally, §4.4 contains a discussion of the results and our conclusions.

4.2 General Results

We list the results of our simulations in Table 4.1. We obtained V^2, B^2, ϵ, and D_M by averaging over (t_1, t_2) using all available data. However, $T_{v|v_2}$ ($\equiv T_{v|v_k}(k = 2)$) and $T_{b|v_2}$ ($\equiv T_{b|v_k}(k = 2)$) were calculated from a sparse subset of the data. k_e is the energy equipartition wavenumber (equation(4.7)). It is important to note that, unless otherwise noted, these time averages are taken after the turbulence has reached the stationary state. Conclusions based on these averages do not apply to the initial growth phase of the magnetic field.

Note that there is no fundamental difference between *zero* and *weak* external field limits (compare Run 96A and REF4, or Run 64A and REF5). Therefore, when we refer to *weak* external field limits, we are actually referring to *zero* external field limits.

Run	N^3	$\nu = \eta$	B_0^2	V^2	B^2	ϵ	D_M	$T_{v\|v_2}$	$T_{b\|v_2}$	k_e	(t_1, t_2)
REF1	96^3	.0043	10^{-4}	.773	.169	.167	.088	.0815	.0353	-	(500,560)
REF2	64^3	.015	-	0.85	-	.163	-	-	-	-	(300,750)
REF3	96^3	.0043	-	1.053	-	.160	-	-	-	-	(50,165)
REF4	96^3	.0043	0	.766	.165	.164	.086	-	-	-	(200,500)
REF5	64^3	.0074	0	.784	.115	.165	.064	-	-	-	(300,800)
144A	144^3	hyper	10^{-7}	.649	.420	.161	-	.0519	.0758	8.4	(60,240)
128A	128^3	.003	10^{-7}	.755	.200	.166	.099	.0794	.0421	7.1	(100,210)
96A	96^3	.0043	10^{-7}	.761	.170	.166	.088	.0807	.0364	6.7	(200,500)
72A	72^3	.0064	10^{-7}	.792	.122	.165	.070	.0870	.0276	6.8	(300,800)
64A	64^3	.0074	10^{-7}	.786	.113	.166	.064	.0835	.0257	6.6	(300,800)
64B	64^3	.01	10^{-7}	.794	.0804	.165	.048	.0860	.0019	6.6	(300,750)
64C	64^3	.015	10^{-7}	.808	.0201	.164	.013	.0903	.0046	8.0	(300,800)
64D	64^3	.02	10^{-7}	.774	$< 10^{-4}$	.164	$\sim 10^{-5}$	-	-	-	(300,750)

Table 4.1: Parameters and Results

4.3 Results

4.3.1 Generation of Magnetic Fields

Fig. 4.1 shows time evolution of kinetic and magnetic energy density. All the simulations have similar kinetic energy densities. However, the magnetic energy density obviously depends on the ohmic diffusivity η. After an initial growth phase, the magnetic energy reaches a stationary state. The initial growth rate of the magnetic energy depends on diffusivity. Even though it is not clearly shown in the figure, the initial growth phase consists of two stages for Run 144A, the hyperviscosity run. In the first stage, which begins at t=0 and ends after a few dynamical times, the growth rate is very fast. At this stage the

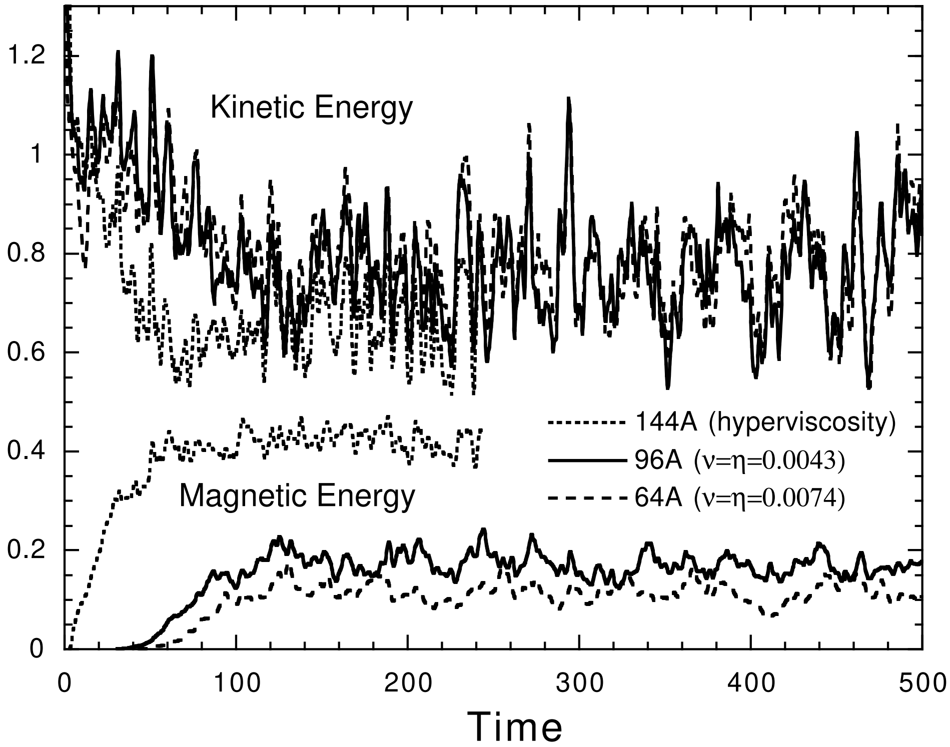

Figure 4.1: Time evolution of kinetic and magnetic energy. The results at three different resolutions are shown: dotted, 144^3 (Run 144A); solid, 96^3 (Run 96A); dashed, 64^3 (Run 64A). For 64A and 96A, the kinetic energy has very similar values. The magnetic energy depends on ν $(= \eta)$. In the case of hyperviscosity (Run 144A), the magnetic energy is more than half of the kinetic energy.

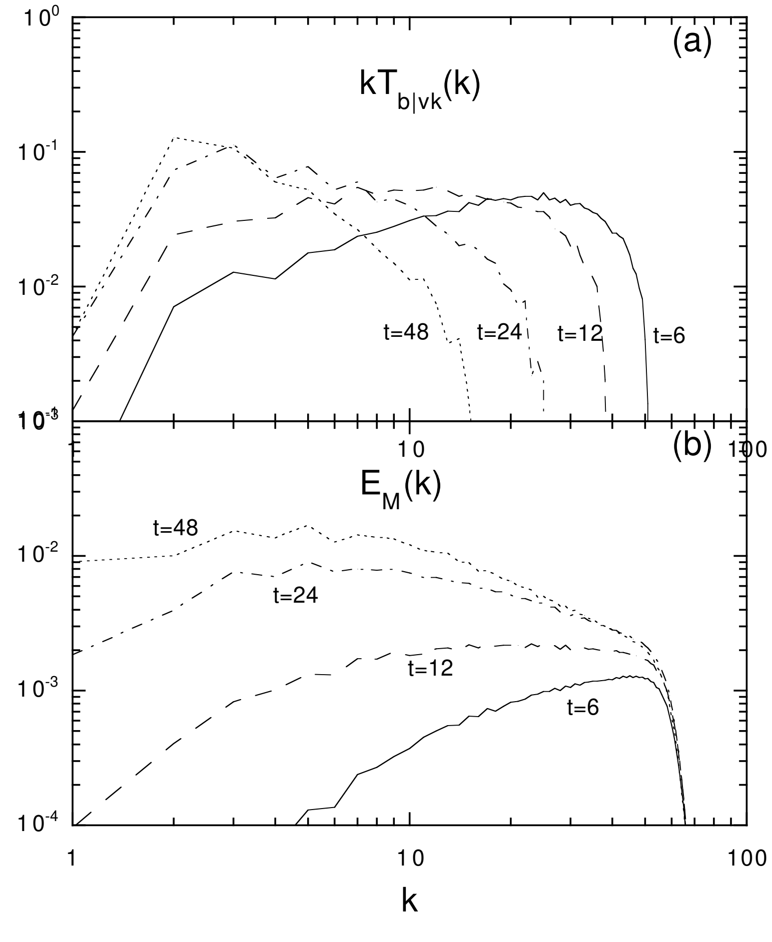

Figure 4.2: Time evolution of $kT_{b|v_k}(k)$ and $E_M(k)$. Run 144A

magnetic energy grows through the stretching of magnetic field lines. Growth is fast because there is no significant back reaction by the magnetic fields. Fig. 4.2 shows that stretching is initially most active near, or somewhat larger than, the dissipation scale (cut-off scale) and the magnetic energy spectrum peaks at this scale. As the magnetic energy grows, the magnetic back reaction becomes important at the dissipation scale. When energy equipartition is reached at this scale, the stretching rate slows down and a second stage of slower growth begins. Fig. 4.2 shows that during this stage the peak of the magnetic power spectrum moves to larger scales. Fig. 4.1 shows the second stage ends at $t = 30 \sim 40$ for Run 144A. Other runs with physical viscosities (Run 128A, 96A, 64A, etc.) also show similar behavior. However, the detailed evolution seems different from the hyperviscosity case. For example, the diffusivity also affects the net growth rate in the second stage.

In Fig. 4.3a, we plot the kinetic and magnetic energy densities as functions of ν $(=\eta)$. Error bars are estimated from

$$2\frac{< X^2 > - < X >^2}{\sqrt{(t_2 - t_1)/t_{corr}}}, \tag{4.1}$$

where $< \cdot >$ denotes the time average and $X = V$ and B. As noted above, this average is taken after the turbulence has reached its stationary state. The correlation time $t_{corr} \sim 3$ is calculated directly. We see that the kinetic energy is almost independent of ν $(=\eta)$. The constancy of the kinetic energy density is the result of the magnetic field. In purely hydrodynamic simulations the kinetic energy density increases as ν decreases (see REF2 and REF3 in Table 4.1). On the other hand, the magnetic energy increases as ν $(=\eta)$ decreases.

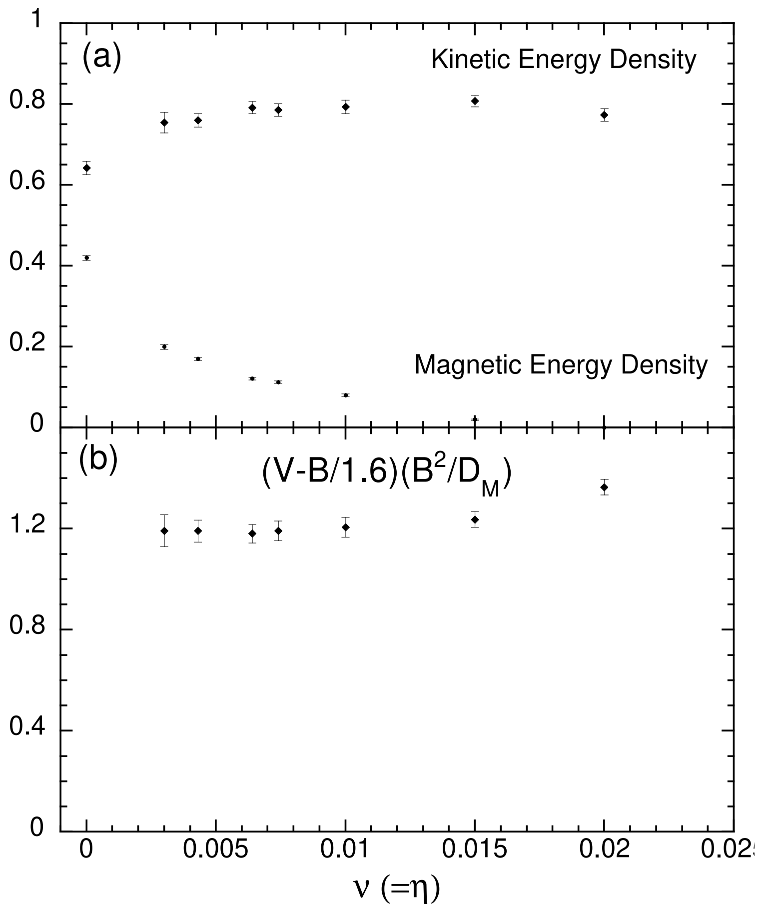

Figure 4.3: Dependence of physical quantities on ν $(=\eta)$. *Top*: The kinetic energy density is nearly independent of the physical viscosity. The magnetic energy density grows as ν $(=\eta)$ decreases. *Bottom*: This relation implies $D_M \sim (V - B/1.6)B^2$.

This figure suggests that at small η even a weak diffuse magnetic field can lead to a strong final state. In the case of hyperviscosity, the magnetic energy is almost half of the kinetic energy at late times. This is the result of field line stretching, and not the alpha effect (see next paragraph and §4.4). The energy injection rates ϵ ($\equiv \mathbf{f} \cdot \mathbf{V} = D_K + D_M$) are independent of ν ($= \eta$) and in the range $0.161 < \epsilon < 0.166$ (Table 4.1).

In Fig. 4.3b, we plot an empirical relation for the generation of magnetic fields in the stationary state:

$$D_M \sim \left(\frac{V}{L} - c\frac{B}{L}\right) B^2, \tag{4.2}$$

where c is a constant (~ 0.63). Since it is not easy to estimate the true amount of magnetic dissipation for Run 144A, we are not sure whether or not this relation is true in the limit of vanishing diffusivity[3]. What is the origin of this correlation? In the stationary state, the magnetic dissipation (D_M) is balanced by the net energy transferred to the magnetic fields from the velocity fields.

[3] In Run 144A, the magnetic dissipation is given by $\sum \nu_8 k^{16} |\hat{\mathbf{B}}|^2$. Although we can calculate this quantity directly, we may not use this for equation (4.2). The reason is as follows. D_M in equation (4.2) actually represents the amount of energy transferred to the magnetic field. If we use a physical viscosity (and diffusivity), the two quantities are same. However, in hyperviscosity runs, the two quantities are not necessarily same because the nonlinear processes occurring near the dissipation cut-off are presumably unphysical. The dotted curve in Fig. 4.4 represents the amount of energy transferred to the magnetic field in Run 144A. The curve shows a non-negligible change after the dissipation cut-off ($k_d \sim 50$), which means that nonlinear processes do occur within the dissipation range (i.e. $k > k_d$). If we take the value of $\Pi_{b|v_k}$ at $k \sim k_d$ for D_M and substitute it into equation (4.2), then we obtain $(v - B/1.6)B^2/D_M = 1.24$. This result is in very good agreement with other data shown in Fig. 4.3b. Then, we can say that equation (4.2) is is true even in the limit of vanishing viscosity (and diffusivity). However, without the knowledge of the nonlinear processes near the dissipation range, this conclusion will be premature.

The right-hand side therefore tells us that the net energy transferred to the magnetic fields is proportional to large-scale eddy turnover rate (V/L) minus an Alfvénic frequency (B/L) times a constant. The large-scale eddy turnover rate is equal to the stretching rate of the magnetic field when the back reaction is zero. We identify the second term on the right-hand side of this equation as the effect of the magnetic back reaction.

This interpretation is supported by the spectrum of the energy transfer rate, $T_{b|v_k}(k)$. The function $T_{b|v_k}(k)$ is the energy lost by velocity components within a unit shell of radius k in wavevector space through interactions with the magnetic field. When this quantity is positive, it means that energy is being transferred from velocity components in the unit shell to the magnetic field. In Fig. 4.4a, we plot $T_{v|v_k}(k)$, $T_{b|v_k}(k)$ and $T_{v|b_k}(k)$ for Run 144A. From the spectrum of $T_{b|v_k}(k)$ we can see that magnetic fields are driven by energy extracted from the large scale velocity components (cf. Kida et al. 1993). We can explain this result if we suppose that the magnetic field energy is generated by field line stretching at large scales. On the other hand, the magnetic fields have a small rate of net energy transfer to small scale motions, implying that on small scales the turbulent motions can be described as nonlinear Alfvén waves, with a rough balance between kinetic and magnetic energy densities.

In Fig. 4.4b, we plot the spectra of energy fluxes. The energy flux $\Pi_{b|v_k}(k)$ is the amount of energy transferred from velocity components whose wavenumbers are less than or equal to k to the magnetic components of all

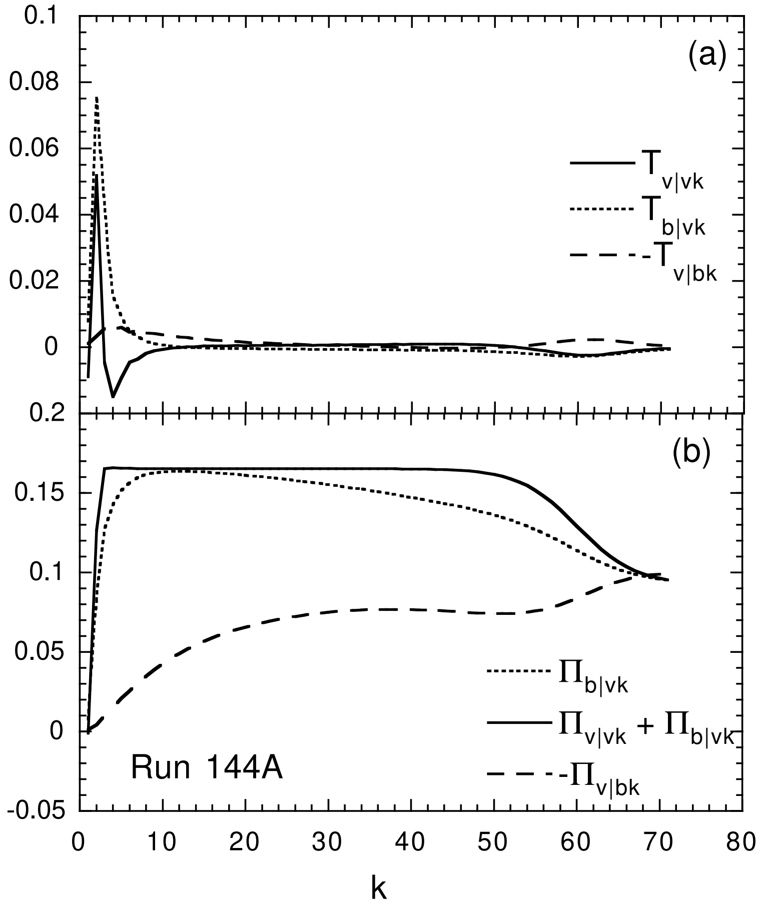

Figure 4.4: Energy transfer and flux spectra for Run 144A. *Top*: Energy transfer spectra. The spectrum of $T_{b|v_k}$ (dotted line) shows that magnetic fields gain energy from large scale eddies. *bottom*: Energy flux spectra. The spectrum of $\Pi_{b|v_k}$ (dotted line) rises rapidly at small k and reaches the value of ϵ at $k \sim 10$.

wavenumbers:

$$\Pi_{b|v_k}(k) = \int_0^k T_{b|v_p}(p)dp. \tag{4.3}$$

We define other fluxes similarly. The graph of $\Pi_{b|v_k}(k)$ rises rapidly at large scales ($k < 10$) and reaches the value of energy injection rate ϵ (~ 0.16) at $k \sim 10$. This means that the energy injected to drive the turbulence (~ 0.16 per unit time) is absorbed at large scales by the magnetic fields. On smaller scales ($k > 10$) the velocity field does not drive the magnetic fields, but instead *absorbs* energy. In summary, the rise of $\Pi_{b|v_k}(k)$ at small wavenumbers is due to field line stretching and the decrease at large wave numbers is a sign of Alfvénic turbulence at small scales. Consequently, at small scales, we can treat the turbulent motions as fully developed MHD turbulence, even when external fields are weak.

Before proceeding, it is useful to take note of a property of hyperviscosity simulations. The quantity $\Pi_{v|v_k}(k) + \Pi_{b|v_k}(k)$ is the total energy transferred from large scale velocity fields ($|\mathbf{k}| < k$) to either magnetic fields or small scale velocity fields. When there is no dissipation, the energy injected by the driving force is either transferred to magnetic fields or transferred to small scale velocity fields:

$$\epsilon = \Pi_{v|v_k}(k) + \Pi_{b|v_k}(k). \tag{4.4}$$

That is, the quantity $\Pi_{v|v_k}(k)+\Pi_{b|v_k}(k)$ has to be a constant for a hyperviscosity simulation. In fact, in the hyperviscosity simulation (Run 144A), this quantity is constant for $k < 50$.

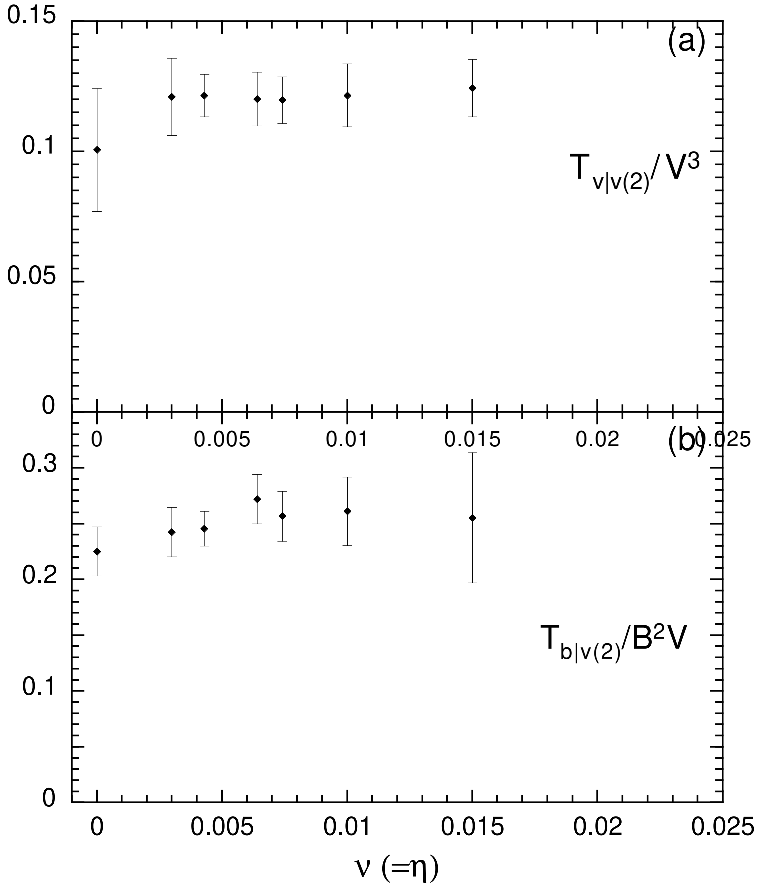

Figure 4.5: Evidences that large-scale turbulence is similar to ordinary hydrodynamic turbulence. *Top*: $T_{v|v_k}(k=2)/V^3$ is nearly constant for nonzero physical viscosity, which implies that $T_{v|v_k}(k=2) \sim V^3$. In the case of hyperviscosity, this relation may not hold true. *Bottom*: $T_{b|v_k}(k=2)/(B^2V)$. This relation implies stretching of magnetic field lines without significant back reaction is responsible for the nonlinear energy transfer from velocity components at $k \sim 2$ to magnetic fields.

In Fig. 4.5, we plot $T_{v|v_2}$ and $T_{b|v_2}$. Here $T_{v|v_2}$ ($\equiv T_{v|v_k}(k = 2)$) is proportional to the rate at which the energy of large scale eddies is transferred to small scale velocity fields. On the other hand, $T_{b|v_2}$ ($\equiv T_{b|v_k}(k = 2)$) is proportional to the rate at which energy of large scale eddies is transferred to magnetic fields. Note that $k = 2$ corresponds to the scale of largest energy containing eddies. Fig. 4.5a shows

$$T_{v|v_2} \sim V^3, \tag{4.5}$$

which suggests that large scale kinetic energy (V^2) is transferred to smaller scales within an eddy turnover time (L/V). That is, turbulence at large scale is broadly similar to ordinary hydrodynamic turbulence and the classical energy cascade model seems to work. In the case of hyperviscosity, the figure suggests that the energy transfer rate may not exactly follow the scaling relation given above. However, as we can see in the figure, the deviation, if any, will be very small.

Fig. 4.5b shows

$$T_{b|v_2} \sim B^2 V. \tag{4.6}$$

When magnetic field is generated through stretching of field lines, $T_{b|v_2}$ will be proportional to the stretching rate at large scales. Although equation (4.2) implies that overall stretching rate is proportional to ($V - const \cdot B$), Fig. 4.5b suggests that the stretching rate scales as B^2V at the largest energy containing eddy scale. That is, it is proportional to the large eddy turnover rate V/L.

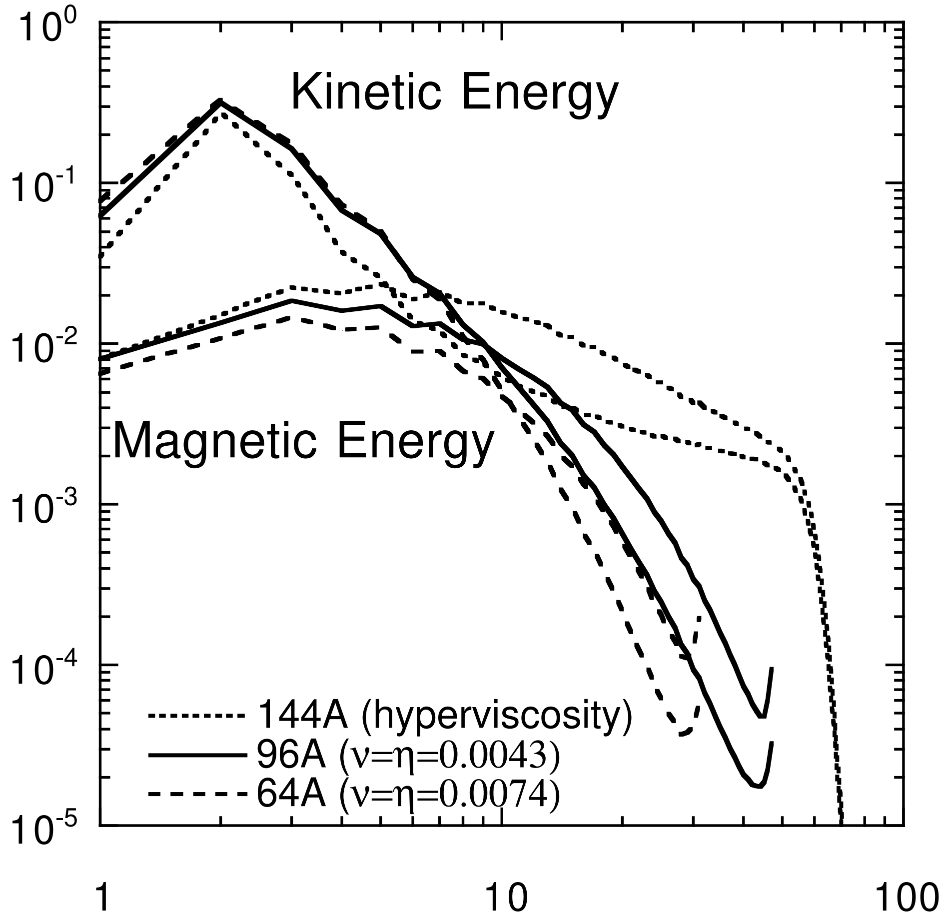

Figure 4.6: Energy spectra. The results at three different resolutions are shown: dotted, 144^3 (Run 144A); solid, 96^3 (Run 96A); dashed, 64^3 (Run 64A). Both axes are drawn in logarithmic scale.

4.3.2 The Structure of Turbulence

We plot energy spectra in Fig. 4.6. For all simulations using physical viscosities (runs 128A, 96A, 72A, and 64A-D) the kinetic energy spectra are almost independent of ν at large scales ($k < 10$). However, this is not true in the case of hyperviscosity (Run 144A). Magnetic energy spectra peak near, but somewhat smaller than, the energy injection scale. The position of the peaks depends on magnetic diffusivity. We see that the location of the peaks moves towards the largest scale as diffusivity increases. In the case of hyperviscosity (and hyperdiffusivity) simulation, both kinetic and magnetic spectra show the well known bottleneck effect (see, for example, Borue and Orszag 1996) for $k >\sim 20$. This effect is characterized by a local enhancement of the energy spectra at scales somewhat larger than the dissipation cutoff.

We define the energy equipartition wavenumber k_e such that

$$\int_0^{k_e} dpE_M(p) = \int_{k_e}^{k_{max}} dpE_K(p). \tag{4.7}$$

In this definition, energy equipartition between *large* scale magnetic fields and *small* scale velocity fields occurs at $k = k_e$. (Therefore, k_e is different from the scale of equipartition between *small* scale magnetic energy and *small* scale kinetic energy. A good measure for the equipartition scale between small scale energies is the wavenumber at which $E_K(k) = E_M(k)$. In the case of hyperviscosity, the two wavelengths are similar.) From Table 4.1, we can see that k_e is not very sensitive to the value of viscosity. In all cases, the equipartition scale ($\sim 1/k_e$) is somewhat smaller than the peak of the kinetic energy spectrum

$(1/k_L \sim 1/2.5)$. The magnetic fields associated wavenumbers greater than k_e act like a strong uniform external magnetic field for eddies smaller than $\sim 1/k_e$, and the structure of turbulence at smaller scales will be similar to Alfvénic turbulence. On the contrary, turbulence at scales larger than $\sim 1/k_e$ will be more or less like ordinary hydrodynamic turbulence. This argument is supported by the fact that the value of k_e is very close to the peak of $\Pi_{b|v_k}(k)$ for all runs. For example, Fig. 4.4b shows $\Pi_{b|v_k}(k)$ peaks at $k \sim 10$ for Run 144A. Table 4.1 shows that $k_e \sim 8.4$ for the same run. (Our analysis also shows that, for Run 96A, $k_e \sim 6.7$ and $\Pi_{b|v_k}(k)$ peaks at $k \sim 8$. And, for Run 64A, $k_e \sim 6.6$ and $\Pi_{b|v_k}(k)$ peaks at $k \sim 8$...) This suggests that, below the equipartition scale, the turbulent fluid is in a state of nonlinear Alfvénic turbulence, with a fixed ratio between the kinetic and magnetic energies associated with perturbations on these scales.

We see that a small external field leads to local magnetic energy density which, in the limit of very small diffusivity, is comparable to the kinetic energy density, with a typical scale only slightly smaller than the scale at which the turbulence is driven. This still leaves the question of whether the magnetic field is characterized by numerous polarity reversals within each eddy. We have examined this question by considering the magnetic field second order structure function. A detailed description of our method can be found in Chaper 3. Here we note only that we define the structure function in cylindrical coordinates as

$$F(\rho, z) = \langle < |\mathbf{Y}(\mathbf{r}_1) - \mathbf{Y}(\mathbf{r}_2)|^2 \rangle, \tag{4.8}$$

where $\mathbf{Y}$ can be either the magnetic field or the velocity. The coordinates are defined relative to the *local* field direction, with ρ being the distance perpendicular to $(\mathbf{B}(\mathbf{r}_1) + \mathbf{B}(\mathbf{r}_2))/2$ and z the distance parallel to it.

We plot the results for run 144A in Fig. 4.7. The shape of the contours represents the average shape of the eddies, which in turn reflects the degree of anisotropy along the local field direction. As expected, the velocity field shows isotropy at large scales and anisotropy at small scales. The magnetic fields show an insignificant amount of correlation at large scales and strong anisotropy at small scales. At intermediate scales, comparable to the equipartition scale, the magnetic field shows a factor of two difference in correlation lengths along local field line directions and across them. The implication is that the field is *not* composed of numerous parallel fibrils with frequent polarity reversals on small scales, as envisioned by Batchelor (1950) and Kazantsev (1967). Instead, the field is largely smoothed by small scale turbulent diffusion, and shows only one or two polarity reversals at its typical scale of organization.

4.4 Discussion and Conclusions

We have presented results of MHD numerical simulations for unit magnetic Prandtl number (i.e. $\nu = \eta$). A weak diffuse magnetic field was used as an initial condition, and we tested the sensitivity of our results to dissipative effects by varying the viscosity and numerical resolution in our simulations. We have found that magnetic fields are amplified through field line stretching at a rate proportional to $(V - cB)/L$, where $c \sim 0.63$. It is not certain whether or not the hyperviscosity run follows this relation. We have also shown that, in the

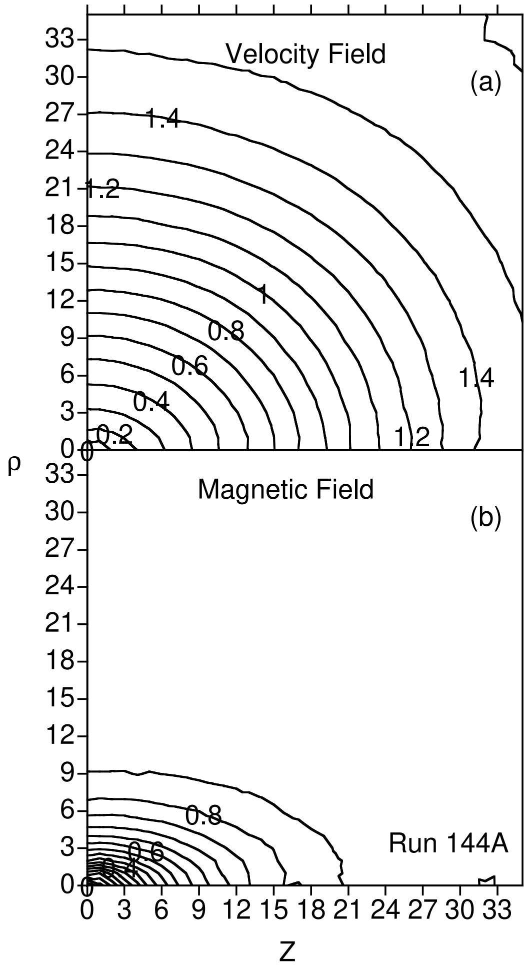

Figure 4.7: Second order structure functions for the magnetic and velocity fields. The horizontal axis is in the direction of the local magnetic field, defined by pairwise averaging. The velocity fields show correlations at all scales, with a smooth transition from isotropy on large scales to anisotropy on small scales. The magnetic field shows similar behavior on small scales, below the equipartition scale, but has almost no correlation on large scales.

limit of ν $(= \eta) \to 0$, the magnetic field reaches a final stationary state where the magnetic energy density is comparable to the kinetic energy. Since the simulations using physically realistic functional forms for the diffusivity are very far away from this limit, we are not able to extrapolate to a definite final ratio of E_B/E_K, but it should be at least as large as the value reached in run 144A, ~ 0.6. The typical scale of the magnetic field is slightly smaller than the scale of the largest energy containing eddies. At or above the equipartition scale, eddies are almost isotropic. However, eddies smaller than the equipartition scale show elongation along the local magnetic field lines.

When we vary viscosity (and diffusivity) explicitly, physical quantities scale as follows:

1. $V^2 \sim$ const
2. $D_M \sim (V - cB)B^2$, c=constant
3. $T_{v|v_k}(k=2) \sim V^3$
4. $T_{b|v_k}(k=2) \sim VB^2$.

The turbulent dynamo effect did not play a role in these simulations. There is no sign of the spontaneous generation of a large scale field, above what we would expect by extrapolating the magnetic energy power spectrum to wavenumbers smaller than the energy peak. Our results are most plausibly explained in terms of random field line stretching within eddies. We have tested this conclusion by conducting additional simulations with no imposed helicity.

The results were almost identical to the simulations presented here. However, this does not allow us to draw any general conclusions about the possibility of mean-field dynamos in astrophysical objects. We note that the average helicity for all the runs listed in Table 4.1 is in the range 0.3 to 0.4. Since the smallest allowable wavenumber is 1, this implies a maximum mean-field growth rate of order 0.1 times the eddy correlation time. By comparison, the turbulent dissipation rate is $\langle V^2 \rangle/3$ (or ~ 0.3) times the eddy correlation time. The obvious conclusion is that no dynamo effect is expected. The energy injection scale here is too close to the size of the computational box.

The isotropic structure of eddies at large scales in our simulations implies something about diffusive processes in MHD turbulence. In particular, it suggests the presence of an effective magnetic diffusivity which is tied to the large scale eddy size rather than the resistive scale. This is an old idea (see, for example, Parker 1955), and is equivalent to the notion that the usual turbulent diffusion coefficients can be substituted for ohmic resistivity. In its original form it was based on a picture of small scale field line mixing, which has been convincingly criticized by Parker (1992). However, it can also be justified by appealing to rapid reconnection, that is, field line reconnection at rates which are comparable to an eddy turn over rate and much more rapid than estimates based on the Sweet-Parker reconnection rate (Sweet 1958, Parker 1957). In terms of our simulations, we note that if reconnection is slow than we expect that magnetic fields will show a thin fibril structure in the saturated state, with a typical field reversal scale much smaller than the curvature scale. We see from the structure function that this is not the case. Apparently, in our simulations at least, reconnection is fast enough to relax tangled magnetic field structures in no more than an eddy turn over time. Either the suppression of reconnection appears suddenly at higher resolutions, or theoretical arguments suggesting fast reconnection in highly conducting turbulent fluids (Lazarian and Vishniac 1999) are correct. If the latter interpretation holds up, then arguments suggesting the suppression of the α effect (e.g. Vainshtein and Cattaneo 1992) at high Reynolds numbers are unlikely to prove correct.

In what follows, we will give a rough explanation for the dependence of field quantities on ν (=η). Readers are advised that this analysis might fail in the limit of vanishing diffusivity. The reason is that run 144A shows slight deviations from the extrapolation results (see V^2 in Fig. 4a and $T_{b|v_2}$ in Fig. 6a). However, in most cases, the deviation is small.

The kinetic energy depends on both viscosity and magnetic energy. The result shown in Fig. 4a that the kinetic energy is almost independent of $\nu = \eta$ is actually the result of a rough cancellation between these two competing effects. Suppose that magnetic field is turned off and, therefore, the turbulence is ordinary hydrodynamic turbulence. Let us also suppose that the viscosity is zero. Then, at the energy injection scale, we will have

$$V^3 \sim \epsilon. \tag{4.9}$$

This is a well known relation in Kolmogorov phenomenology wherein the energy injection rate ϵ is equal to the energy cascade rate at the largest energy containing scale, which is proportional to the energy contained in the largest eddies ($\sim V^2$) divided by one eddy turnover time ($\sim L/V$). When viscosity is not extremely small, we need to add a viscosity effect:

$$V^3 + \nu V^2 \sim \epsilon, \tag{4.10}$$

where we omit constants of order unity in each term. The second term in left-hand side is proportional to dissipation at the large scale. Since the second term on the left-hand side is much smaller than the first, we can assume that $\nu V^2 \propto \nu + O(\nu^2)$. If we solve this relation for V^2, we obtain

$$V^2 \sim C_\epsilon \epsilon^{2/3} - C_\nu \nu, \tag{4.11}$$

where the C's are constants. Now if we turn on the magnetic fields and set the viscosity to be zero, then we have

$$V^3 + B^2 V \sim \epsilon. \tag{4.12}$$

Here we also omit constants of order unity in each term. The first term in left-hand side is still proportional to V^3, which is supported by the relation $T_{v|v_2} \propto V^3$ (Fig. 6a). The second term in left-hand side comes from the relation $T_{b|v_2} \propto VB^2$ (Fig. 6b). Since the second term is small compared with the first, we can write $B^2 V \propto B^2 + O(B^4)$. Solving for V^2, we have

$$V^2 \sim C_\epsilon \epsilon^{2/3} - C_B B^2. \tag{4.13}$$

If we combine the two relations, we have

$$V^2 \sim C_\epsilon \epsilon^{2/3} - C_\nu \nu - C_B B^2, \tag{4.14}$$

where we ignore the interactions between ν-effect and B^2-effect. If any, such interactions will be weak because both ν-effect and B^2-effect are weak. This equation implies that the quantity $V^2 + C_B B^2$ depends only on ν.

To complete above analysis, we need an expression for B^2. To this end, let us adopt an energy cascade model analogous to ordinary hydrodynamical case: The energy $transfer$ rate is equal to $magnetic$ energy cascade rate at the large scale. The energy transfer rate is given in equation (4.2). The magnetic energy cascade rate is $B^2/(L/V)$. Therefore, we have

$$(V - B)B^2 \sim B^2 V + \eta B^2, \tag{4.15}$$

where the second term in right-hand side is the large scale dissipation term. Again, we omit all order unity constants. If we solve the equation for B, we obtain

$$B = C_V V - C_\eta \eta, \tag{4.16}$$

where C's are constants. In fact, our calculation shows that

$$\frac{B - 0.6V}{\eta} = -26.7 \pm 2.1, \tag{4.17}$$

for Runs 128A, 96A, 72A, 64A, 64B, 64C, and 64D. It implies that $C_V = 0.6$ and $C_\eta \sim 26$. This relation slightly underestimates the magnetic field strength for Run 144A. (It gives $B \sim 0.6V$, as opposed to the observed value of $0.8V$.) If we examine Fig. 4.6 we see that this discrepancy arises from the difference between the rms magnetic field strength, and the magnetic field strength on the largest eddy scale. Comparing the hyperviscosity run (144A) with the other cases we see that the former has a substantially greater fraction of its magnetic energy in small scale structures. If we interpret B in the preceding equation as the average obtain by smoothing on the large eddy scale, which is consistent with our derivation, then the hyperviscosity run is in agreement with equation (4.17). In this sense, the values of B and B^2 present in this discussion section should be regarded as lower limits for the case of vanishing diffusivity. Alternatively, one might regard the following discussion as valid for cases of moderate magnetic Reynolds numbers and that this analysis sets limits for the case of zero diffusivity. For B^2, we have

$$B^2 \sim C_V^2 V^2 - 2C_V C_\eta V \eta. \tag{4.18}$$

Here we omitted $C_\eta^2 \eta^2$ in right-hand side.

If we combine expressions for V^2 and B^2, we have

$$V^2 \sim (C_\epsilon \epsilon^{2/3} - C_\nu \nu + C_\eta \eta)/(1 + C_B C_V^2), \tag{4.19}$$

$$B^2 \sim (C_V^2 C_\epsilon \epsilon^{2/3} - C_V^2 C_\nu \nu - C_V C_\eta V \eta)/(1 + C_B C_V^2). \tag{4.20}$$

Note that, even though we treat ν and η separately, there is no guarantee that above relations are true for non-unity Prandtl numbers. Since $\nu = \eta$ and the second and third terms in right-hand side of equation (4.19) have different signs, V^2 depends on ν ($=\eta$) weakly. We expect C_B and C_V have similar values, because they are describing similar things - dissipation. The expression for B^2 is not absolutely correct because the omitted term in equation (4.18) becomes non-negligible when η becomes large.

When $\nu = \eta = 0$, we have

$$V^2 \sim C_\epsilon \epsilon^{2/3}/(1 + C_B C_V^2), \tag{4.21}$$

$$B^2 \sim C_V^2 C_\epsilon \epsilon^{2/3}/(1 + C_B C_V^2). \tag{4.22}$$

These give a lower limit for B^2 and an upper limit for V^2.

Chapter 5

Summary and Future Works

In summary, we have investigated the structure of MHD turbulence in two extreme regimes: strong external magnetic field regime and weak/zero external magnetic field regime.

When the external magnetic field is greater than rms velocity, numerical results confirm the proposal of Goldreich and Sridhar (1995, 1997) that smaller eddies are relatively more elongated along the direction of the local magnetic field lines than larger ones. The proposed criteria that hydrodynamic and Alfvénic rates should be roughly equal at all scales is also confirmed, although with some margin of error.

When the external field is weak/zero, we found that the scale of energy equipartition can be used for reference scale for anisotropy. At or above the equipartition scale, eddies are almost isotropic. However, eddies smaller than the equipartition scale show elongation along the local magnetic field lines. We have also found that magnetic fields are amplified through field line stretching at a rate proportional to $(V - cB)/L$, where $c \sim 0.63$. It is not certain whether or not the hyperviscosity run follows this relation. We have also shown that, in the limit of ν $(= \eta) \to 0$, the magnetic field reaches a final stationary state where the magnetic energy density is comparable to the kinetic energy.

Throughout this work, we assumed that astrophysical plasmas are good fluids. That is certainly true in stars and accretion disks, not terribly true in coronae (either stellar or disk), and false in the interstellar medium. The fluid approximation is usually true when mean free path of particles is much shorter than the characteristic length scale of the system being considered. When this condition is violated, we can no longer describe the system through the large-scale collective behavior. Instead, we may need the Boltzmann equation to describe the behavior of particles. Therefore, we should be careful when we apply our results (and Goldreich and Sridhar's model) to such a system. Nevertheless, observations of the solar wind and the density irregularities in the interstellar medium (throuth interstellar scintillation) suggest that this model seems to work even in the very low density environments.

In this work, we have not included the regime of a B_0 of intermediate strengths. We are currently working on this regime. The regime of extremely strong B_0 limits will also be an interesting topic. All the discussions in this work is for incompressible fluids. It will also be interesting to reproduce these simulations for compressible fluids for Alfvén velocities close to the sound speed..

Bibliography

[1] Armstrong, J.W., Rickett, B.J., and Spangler, S.R. 1995, ApJ, 443, 209

[2] Batchelor, G., 1950, Proc. R. Soc. Lond., A 201, 405

[3] Borue, V. and Orszag, S.A., 1995, Europhys. Lett., 29(9), 687

[4] Borue, V. and Orszag, S.A., 1996, J. Fluid Mech., 306, 293

[5] Brandenburg, A., Procaccia, I. and Segel, D., 1995, Phys. Plasmas, 2 (4), 1148

[6] Cho, J. and Vishniac, E. T., 2000, ApJ accepted (astro-ph/0003403)

[7] Fournier, J., Sulem P. and Pouquet, A., 1982, J. Phys. A, 15, 1393

[8] Ghosh, S. and Goldstein, M.L., 1997, J. Plasma Physics, 57, 129

[9] Goldreich, P. and Sridhar, H., 1995, ApJ, 438, 763

[10] Goldreich, P. and Sridhar, H., 1997, ApJ, 485, 680

[11] Iroshnikov, P., 1963, Astron. Zh., 40, 742 [1963, Sov. Astron., 7, 566]

[12] Kazantsev, A.P. 1967, JETP, 53, 1806

[13] Kida, S., Yanase, S. and Mizushima, J., 1991, Phys. Fluids A, 3(3), 457

[14] Kraichnan, R., 1965, Phys. Fluids, 8, 1385

[15] Lazarian, A., and Vishniac, E.T., 1999, ApJ, 517, 700

[16] Leamon, R. J., Smith, C. W., Ness, N. F., Matthaeus, W. H. and Wong, H. K., 1998, J. of Geophys. Res., 103, 4775

[17] Maron, J. and Goldreich, P. 1999, private communication

[18] Matthaeus, W.H., Oughton, S., Ghosh, S. and Hossain, M., 1998, Phy. Rev. Lett. 81, 2056

[19] Montgomery, D.C. and Matthaeus, W.H., 1995, ApJ, 447, 706

[20] Moffatt, H. K., 1978, Magnetic Field Generation in electrically Conducting Fluids (Cambridge: Cambridge Univ. Press)

[21] Ott, E., 1998, Phys. Plasmas, 5(5), 1636

[22] Oughton, S., Priest, E.R. & Matthaeus, W.H. 1994, J. Fluid Mech., 280, 95

[23] Parker, E.N. 1955, ApJ, 122, 243

[24] Parker, E.N. 1957, J. Geophys. Res., 62, 509

[25] Parker, E. N., 1979, Cosmical Magnetic Fields (Oxford: Oxford Univ. Press)

[26] Parker, E.N. 1992, ApJ, 401, 137

[27] Pouquet, A. Frish, U. and Léorat, J., 1976, J. Fluid Mech., 77, 321

[28] Shebalin J.V., Matthaeus, W.H. and Montgomery, D., 1983, J. Plasma Phys., 29, 525

[29] Sweet, P.A. 1958, in IAU Symp. 6, Electromagnetic Phenomena in Cosmical Plasma, ed. B. Lehnert (New York: Cambridge Univ. Press), 123

[30] Vainshtein, S. I. and Cattaneo, F., 1992, ApJ, 393, 165

[31] Vishniac, E. T., 1995a, ApJ, 446, 724

[32] Vishniac, E. T., 1995b, ApJ, 451, 816

Vita

Jungyeon Cho was born in Sang-joo, South Korea on March 11, 1966, a son of Nam-Wook Cho and Ok-Ja Shin. After completing his work at Kyunghee High School, Seoul, South korea, in 1984, he entered Seoul National University, South Korea. He received B.S. in Astronomy in 1988 and M.S. in Astronomy in 1991 from the university. He was drafted by the Korean Army in 1991 and discharged from the army in 1992. In September 1993, he entered the Graduate School of the University of Texas.

Permanent address: 230-3 Joong-gok Dong
Kwang-jin Gu, Seoul
South Korea

This dissertation was typeset by the author.